

Contents lists available at ScienceDirect

International Journal of Plasticity

journal homepage: www.elsevier.com/locate/ijplas





Uncovering origin of grain boundary resistance to irradiation damage in NiCoCr multi-principal element alloys

Fusheng Tan^a, Jia Li^{a,*}, Bin Liu^b, Peter K Liaw^c, Qihong Fang^{a,*}

- ^a State Key Laboratory of Advanced Design and Manufacturing Technology for Vehicle, College of Mechanical and Vehicle Engineering, Hunan University, Changsha 410082, PR China
- ^b State Key Laboratory of Powder Metallurgy, Central South University, Changsha 410083, PR China
- ^c Department of Materials Science and Engineering, The University of Tennessee, Knoxville, TN 37996, USA

ARTICLE INFO

Keywords: Multi-principal element alloys Grain boundary Irradiation damage Entropy Molecular dynamic simulation

ABSTRACT

Multi-principal element alloys (MPEAs) demonstrate significant promise as structural materials for nuclear energy equipment owing to their exceptional mechanical properties and radiationresistant performances. In these alloys, the grain boundary (GB) serves as a crucial microstructure that typically mitigates irradiation damage by absorbing the irradiation-induced defect. However, the micromechanisms governing the anti-irradiation performance of GBs in MPEAs remain unclear. In this study, we investigate the irradiation defect production during collision cascade in the model NiCoCr bicrystal system through atomic simulations, aiming to unveil the atomic-scale origin of GB to resist irradiation damage in MPEAs. The results reveal that GBs effectively serve as sinks for irradiation defects in NiCoCr. The sink efficiency depends on the GB energetic state, including GB excess energy and defect segregation energy, as well as the energetic difference between interstitial and vacancy segregation. Statistical analysis identifies a universally exponent function between the defect absorption rate at GB and GB energetic state. In NiCoCr, the GB-disorder-induced-entropy increase leads to a biased reduction in interstitial segregation energy, narrowing the gap between interstitial and vacancy segregation energies by approximately 11 % compared to Ni. This improvement enhances the overall resistance of GBs to irradiation damage. Additionally, preferential segregation of Ni interstitial atoms is notably enhanced in NiCoCr, contributing to a high defect absorption rate at GBs. This study provides new insights into the resistance of GBs to irradiation defects in MPEAs and suggests GB engineering as an effective strategy for developing advanced alloys with enhanced radiation tolerance.

1. Introduction

The rapid expansion of nuclear energy has heightened the demand for improved irradiation resistance in structural materials for nuclear equipment. However, existing alloys have reached their performance limits (Forty and Karditsas, 2000; Knaster et al., 2016), presenting challenges in meeting the evolving needs of future nuclear equipment development. This trend makes it urgent to develop brand-new material systems (Barron et al., 2020; Cui et al., 2018a,b; Cui et al., 2018c; Li et al., 2021; Zhang et al., 2023b). Over the last few decades, multi-principal element alloys (MPEAs) have garnered widespread attention due to their novel compositional design concepts and outstanding mechanical properties (Cao et al., 2023; George et al., 2019; Miracle and Senkov, 2017; Romero et al., 2022;

E-mail addresses: lijia123@hnu.edu.cn (J. Li), fangqh1327@hnu.edu.cn (Q. Fang).

^{*} Corresponding authors.

Wei et al., 2022; Zhang et al., 2014). Many MPEAs exhibit an impressive combination of high strength and ductility in extreme environments, such as at ultra-high temperatures (Senkov et al., 2019, 2010; Wang et al., 2020; Wang and Wang, 2022; Zhou et al., 2016a), at cryogenic temperatures (Ding et al., 2019; Gludovatz et al., 2014, 2016; Naeem et al., 2020; Schneider and Laplanche, 2021), and high-impact scenarios (Jiang et al., 2016; Liu et al., 2020; Peng et al., 2021; Zhang et al., 2017). Notably, several MPEAs with straightforward composition designs exhibit promising irradiation resistance, showcasing low swelling, hardening, and embrittlement under irradiation (Chen et al., 2020b; Deluigi et al., 2021; Ji et al., 2022; Lu et al., 2016; Moghaddam et al., 2021; Patel et al., 2020; Sadeghilaridjani et al., 2020; Zhang et al., 2022b). A thorough exploration of the expansive compositional design space and unique microstructures of MPEAs holds the potential for a sustainable breakthrough in irradiation performance.

To achieve a systematic design of composition and microstructure, it is imperative to unveil the underlying mechanisms. The current body of research predominantly focuses on probing the impact of compositions on the irradiation resistance and elucidating the intrinsic mechanisms contributing to the irradiation damage tolerance of MPEAs (Lin et al., 2020; Lu et al., 2016; Zhang et al., 2015b; Zhao, 2020; Zhao et al., 2018; Zinkle and Busby, 2009). Employing a combination of ab initio calculations, atomic simulations, and experiments, it has been unveiled that the composition of MPEAs alters the intrinsic defect properties from the quantum scale to the nanoscale. At the quantum-atomic level, the mixing of multiple elements leads to a short electron mean free path, resulting in slow energy dissipation and low thermal conductivity (Lin et al., 2020; Orhan et al., 2023; Zhang et al., 2015b). Simultaneously, the migration energies of vacancies and interstitials exhibit wide distribution and significant overlap (Roy et al., 2022; Shi et al., 2022; Su et al., 2023; Zhao, 2020; Zhao et al., 2018), enhancing the interaction between vacancies and interstitial atoms. In nanoscale, the randomly distributed elements generate a heterogeneous atomic strain field, transitioning the conventional 1D motion of interstitial clusters into high-frequency 3D motion within a localized area (Lu et al., 2016, 2021; Zhao et al., 2021). These factors significantly boost the recombination of vacancies and interstitial atoms, offering a partial explanation for the enhanced irradiation resistance of MPEAs.

However, the impact of microstructure on irradiation damage in a chemically diverse environment of MPEAs remains unclear. In particular, grain boundaries (GBs) are prevalent crystal defects in alloys, adept at accommodating a significant number of irradiation-induced defects, thereby become a key microstructure to mitigate the irradiation damage (Christodoulou et al., 2023; El-Atwani et al., 2019; Field et al., 2015; Hoffman et al., 2023; Li et al., 2016; van Beers et al., 2015; Zhou et al., 2016b). The high-frequency interaction between GBs and irradiation defects leads to the segregation/depletion of elements (Field et al., 2015; Hoffman et al., 2023; Li et al., 2016; Wen et al., 2020) and further results to the spatially heterogeneous formation of defect clusters, such as dislocation loops, voids, and precipitates (Bao et al., 2022; Field et al., 2017; Gao et al., 2023; Hung et al., 2022; Li et al., 2023e; Xiao et al., 2019; Xie et al., 2023). This interaction proves to be a crucial strategy for mitigating radiation damage in materials. Currently, our understanding of the effect of GBs on the irradiation response of MPEAs is limited and mostly speculative, relying on extrapolations from studies conducted on conventional alloys.

Numerous studies have demonstrated that the anti-radiation ability of GBs varies across different GB types (Barr et al., 2018; Baruffi and Brandl, 2023; Gao et al., 2023; Hung et al., 2022; Li et al., 2023e; Moladje et al., 2022; Pu et al., 2022). Some preliminary studies have explored the connection between the GB structure/energy and anti-irradiation ability (Dunn et al., 2016; Field et al., 2015; Jiang et al., 2014; Li et al., 2014; Tiwari et al., 2019; Xu et al., 2022; Zhu et al., 2023). For instance, the quantitative relationship between GB misorientation and sink strength, which quantifies a sink's efficiency in absorbing defects, has been extensively examined and applied to elucidate irradiation damage in polycrystalline materials (Jiang et al., 2014; Zhu et al., 2018). However, the controlling factor of GBs in inhibiting irradiation damage remains contentious due to the diversity of GB types. This issue is not only prevalent in conventional alloys but is even more pronounced for MPEAs. The mechanism of GB resistance to irradiation damage is more intricate in MPEAs due to the complex chemical environment.

Recent studies have revealed that GB structure, properties, and interactions with other microstructures in MPEAs differ compared to conventional alloys (Eleti et al., 2020; Elsener et al., 2009; Tan et al., 2021; Utt et al., 2020; Yang et al., 2020; Zhang et al., 2023b). For example, the GB structure in MPEAs tends to exhibit roughening and disordering due to complex alloying (Gupta et al., 2007; Li et al., 2022b; Tan et al., 2021). This not only triggers the transition of GB migration mechanisms (Tan et al., 2021), but also enhances their efficiency in healing defect clusters such as stacking fault tetrahedra (Li et al., 2022a, b; Li et al., 2016). It is evident that GB engineering has become a viable option for modulating the microstructure and properties of MPEAs.

To achieve effective anti-irradiation GB engineering, a crucial step is understanding the mechanism behind GB resistance to irradiation damage. The resistance of GBs to irradiation damage originates from the rapid interaction between radiation-induced defects produced by nanoscale collision cascades and GBs. Given the swift nature of this interaction process (10–20 ps), experimentally capturing the nanoscale mechanisms of GB radiation resistance poses a significant challenge. Fortunately, molecular dynamics (MD) simulations have emerged as a powerful tool for modeling collision cascades. They enable the exploration of defect creation and morphology, mutual interactions, and, to some extent (specifically at very short times), their evolution (Becquart et al., 2019).

Currently, MD simulations are widely employed to scrutinize the impact of GBs on radiation damage. Results from cascade collision simulations in pure metals, such as Fe and W, reveal a significantly lower count of surviving defects in bicrystals and nanocrystalline materials compared to single crystals (Liu et al., 2022; Manna and Pal, 2023; Wang et al., 2017; Zhang et al., 2015a), indicating the efficient reduction of irradiation damage by GBs at the early stages of irradiation. Calculations of defect segregation energies on GBs underscore the GB's effectiveness as a sink for irradiation defects, especially for interstitial atoms, with sink strength being sensitive to GB type and composition (Baruffi and Brandl, 2023; Fernández-Pello et al., 2022; Samaras et al., 2003; Zheng et al., 2023; Zhou et al., 2022). When exposed to an excess of irradiation-induced interstitial atoms, GBs can also emit interstitial atoms into the bulk to annihilate vacancies within grains (Bai et al., 2010; Li et al., 2023e, 2022c), affirming GBs as excellent anti-radiation microstructures even under high-dose irradiation. Recent studies have initially explored the influence of GBs on the irradiation damage of MPEAs based

on collision cascades simulations. The results demonstrate that $\Sigma 5$ tilt GBs in NiFe and CoCrCuFeNi are effective sinks for irradiation defects compared to Ni (Li et al., 2023a, 2023c), with sink strength sensitivity to Fe concentration (Li et al., 2023a). Another simulation involving dislocations in FeCoCrNi indicates that the differences between the numbers of dislocation-absorbed interstitials and vacancies in FeCoCrNi are smaller than in Ni (Chen et al., 2023), attributed to the smaller difference in mobilities of interstitials and vacancies. These findings suggest that GBs in MPEAs are effective sinks for irradiation defects. However, these simulations focus on a limited number of GBs, providing an incomplete understanding of the correlation between GB properties and irradiation defect characteristics. Additionally, the impact of GB disordering on sink strength in MPEAs remains unclear. Elucidating the anti-irradiation mechanism of GBs in MPEAs can not only provide a reference for other microstructures, but also serve as a crucial milestone in the development of microstructure design for irradiation-resistant MPEAs.

In this study, we systematically investigate the impact of thirteen representative GBs on the irradiation damage in the model NiCoCr MPEA. The relationships between the GB properties (misorientation, excess energy, excess volume, and defect segregation energy) and the irradiation-damage characteristic (the number of peak defects and surviving defects, and the defect absorption rate) are comprehensively analyzed. A unique correspondence between GB properties and irradiation damage characteristics is identified, shedding light on the anti-irradiation micromechanism of GBs. Through a comparative analysis between NiCoCr and Ni systems, we explore the role of intrinsic severe lattice distortion, GB disordering and specific elements, uncovering the physical origin of the enhanced resistance of GBs to irradiation damage in MPEAs.

2. Method

2.1. General setting and interatomic potential

Atomic simulation is widely applied to capture the material response in the early stages of irradiation, providing its ability to reproduce structural evolution at a nanosecond timescale. In this study, MD simulations are performed to simulate the defect production during the collision cascade caused by high-energy particle incidence in pure Ni and equimolar NiCoCr alloy. All simulations are conducted using the Large-scale Atomic/Molecular Massively Parallel Simulator (LAMMPS) (Plimpton, 1995), and visualization is performed with the Open Visualization Tool (OVITO) software (Stukowski, 2010). The interatomic interaction is described by a potential function based on the embedded-atom-method (EAM) (Li et al., 2019). This potential does not consider the spin polarization, but it adequately captures key features of typical MPEAs, including multi-principal constituents with similar atomic sizes, chemical interactions consistent with MPEA solutions, and a single-phase solution with variable local chemical order. This potential has been widely used for simulating lattice defects in NiCoCr MPEA (Li et al., 2019; Zhang et al., 2023a), and the microstructural evolution is accurately predicted.

Due to the high kinetic energy of incident particles, some atoms close proximity may deviate significantly from equilibrium atomic spacing during cascade, resulting in increased interatomic repulsion. To capture this repulsion, the short-range interatomic interaction is described using the Ziegler–Biersack–Littmark (ZBL) repulsive potential (Ziegler and Biersack, 1985). The transition distance between ZBL and EAM potentials is set at 1.2 Å, closely aligning with the typical cut-off distance range (~1 Å) of the ZBL potential (Manna and Pal, 2023; Nordlund et al., 1998; Xiong et al., 2023). The ZBL potential is widely employed in MD simulations of displacement cascades across various materials, including metals (Liu et al., 2022; Wang et al., 2017) and alloys (Chen et al., 2023; Liu et al., 2022; Xiong et al., 2023), enhancing prediction accuracy for defect production during displacement cascades.

2.2. Modeling and structural optimization

Thirteen distinct GB models with different atomic structures are utilized, as presented in Table 1. These GBs have various tilt axes

Table 1 Basic information of the GBs used in the present work. The GB type, misorientation angle, θ , excess energy, γ_{GB} , and excess volume, V_{GB} , are presented.

		Ni		NiCoCr	
GB type	θ (°)	$\gamma_{GB} (mJ/m^2)$	V_{GB} (Å)	$\gamma_{GB} (mJ/m^2)$	V_{GB} (Å)
$\sum 3[111](112)$	109.47	81.77	-0.013	-31.384	-0.0146
$\sum 5[001](210)$ -a	53.13	1352.10	0.0337	997.403	0.2460
∑5[001](210)-b	53.13	1387.17	0.2003	1000.067	0.2301
$\sum 5[001](310)$ -a	36.87	1519.10	0.0256	1330.903	0.2485
∑5[001](310)-b	36.87	1284.35	0.2237	1033.482	0.2720
\sum 5[001](650)-a	79.6	1947.38	0.3208	799.927	0.1703
∑5[001](650)-b	79.6	1213.16	0.1194	775.530	0.1646
\sum 5[001](750)-a	71.1	1453.94	0.2524	754.270	0.1987
∑5[001](750)-b	71.1	1114.41	0.2177	741.163	0.1977
$\sum 11[110](113)$ -a	50.48	527.14	0.0844	324.683	0.1362
∑11[110](113)-b	50.48	537.80	0.0911	362.801	0.1185
\sum 19[110](331)-a	153.47	1256.12	0.1586	1029.175	0.1566
∑19[110](331)-b	153.47	1296.55	0.2926	1035.085	0.1645
Average		1151.61	0.1544	781.008	0.1761
Standard error		474.05	0.1025	354.410	0.0708

(111, 001, and 110) and misorientation angles (from 36.87° to 153.47°). Considering the fact that most GBs in materials are inherently non-equilibrium and distinguished by differing atomic densities (Cantwell et al., 2014; Han et al., 2016; Tucker and McDowell, 2011), the non-equilibrium GBs are also constructed. To create the non-equilibrium GB model, the atomic density of a GB is adjusted by removing GB atoms within the cutoff distance of 3.0 Å. GBs with the same tilt axes and misorientation but varying atomic densities are denoted by the suffixes "–a" and "–b" in Table 1. Consequently, these GBs exhibit diverse geometrical characteristics and a wide range of structural parameters, providing ample scope for investigating the general principles governing the impact of GBs on irradiation damage. Additionally, single-crystal models of Ni and NiCoCr are constructed for comparative analysis with the results obtained from the bicrystal model, elucidating the influence of GBs.

The simulation boxes have dimensions of approximately $200 \times 200 \times 200$ ų, which is large enough to ensure that the defect evolution is limited in the internal region of the box during collision cascade, and is not affected by the cascade collision in the periodic boxes. The GB is positioned 25 Å below the center of the model, as the primary knock-on atom (PKA) would be selected from the box center and the resulting collision-cascade peak thermal is located near the GB. This configuration aligns with previous simulations (Chen et al., 2023; Wang et al., 2017; Zhang et al., 2015a), and the outcomes remain independent of the box size and GB position.

The representative bicrystal models are depicted in Fig. 1(b-e). In constructing the NiCoCr system, an initial pure Ni model is created, followed by the random replacement of elements with Co and Cr until the desired composition is achieved. This process ensures a homogeneous chemical environment, as evidenced by the similar fractions of atomic pairs in the GB and grain regions (Fig. 1(f-g)). The atomic structure of the initial model undergoes optimization using the conjugate gradient method to attain a locally minimized energetic state. Subsequently, the system is relaxed for 100 ps under the NPT ensemble (10 K, 0 bar) to reach a kinetic steady state. Following this, collision cascade simulations are conducted at 10 K. It is essential to note that the low temperature of 10 K is chosen to eliminate the influence of temperature effects. The influence of temperature would be discussed in the later section. Throughout all simulations, the model maintains a periodic boundary condition in all directions.

After static structural optimization, the GB excess property P_{GB} can be calculated, including the excess energy γ_{GB} , excess volume V_{GB} . The GB excess property is the increment in the property of the bicrystal model and single-crystal model with the same atomic number (Fischer et al., 2019; Zheng et al., 2020, 2023), i.e.,

$$P_{GB} = \left(P_{BC} - N_{BC} \frac{P_{SC}}{N_{SC}}\right) / 2A_{GB} \tag{1}$$

where P_{GB} is the GB excess property, A_{GB} is the area of the GB in the bicrystal model. P_{BC} and P_{SC} are the total atomic properties of bicrystal model and single-crystal model, respectively. N_{BC} and N_{SC} are the atomic number of the bicrystal model and single-crystal model, respectively. When P_{BC} and P_{SC} are equal to the total atomic potential energy of the bicrystal and single-crystal models, P_{GB} equals the GB excess energy γ_{GB} . Similarly, considering the total atomic volume, P_{GB} equals the GB excess volume V_{GB} . The values for excess energy γ_{GB} and excess volume V_{GB} for different GBs are given in Table 1.

2.3. Collision cascade

To simulate the collision cascade, a Ni atom at the center of the model is designated as the PKA and endowed with an initial velocity directed toward the GB, providing the PKA with an initial kinetic energy of 10 keV. The distance between the PKA and GB plane is approximately 25 Å. This distance is meticulously tested and chosen to ensure that the center of the cascade thermal peak closely aligns with the center of the GB. The cascade is conducted under the NVE ensemble, with two thin layers of 10 Å thickness at the upper and

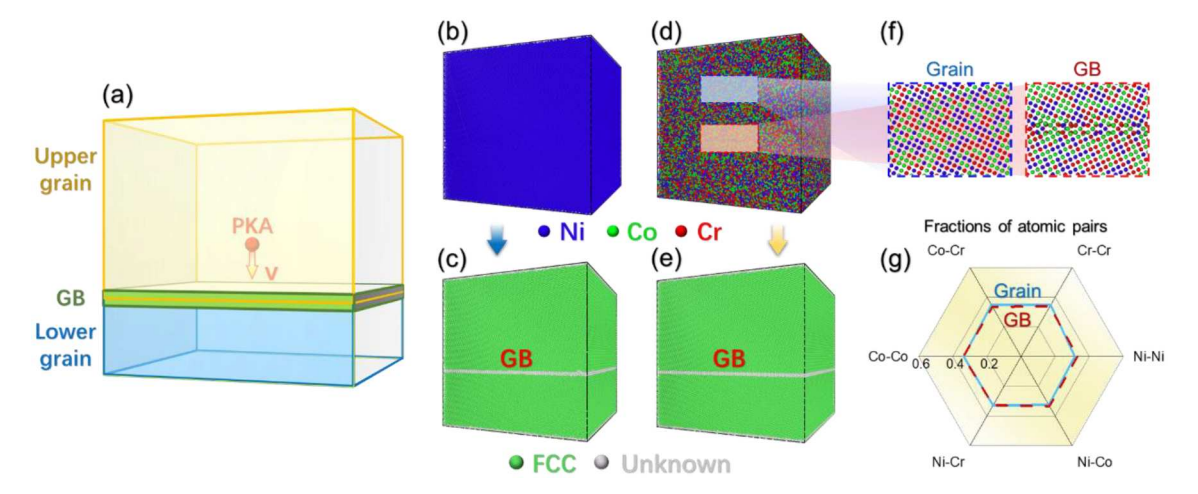


Fig. 1. Simulation method. (a) Schematic image of the bicrystal model and collision cascade simulation. (b) Element distribution and (c) crystalline structure of a representative Ni bicrystal. (d) Element distribution, and (e) crystalline structure of a representative NiCoCr bicrystal. (f) Enlarged images of the atomic details of GB and grain. (g) The fractions of all atomic pairs in the GB and grain regions.

lower boundaries of the simulation box serving as a thermostatic layer, maintaining a constant temperature of 10 K.

The time step during the cascade simulation varies within the range of [0.00001 fs, 0.5 fs] to ensure that the displacement of atoms per timestep does not exceed 0.005 times the lattice constant ($\sim 0.02 \text{ Å}$). The cascade reaction operates for 100 ps to ensure that the system has ample time to reach a steady state following the collision cascade. The simulation duration is sufficiently long to capture stable defects produced by the collision cascade, as validated in prior studies (Chen et al., 2023; Wang et al., 2017; Zhang et al., 2015a), and corroborated by the present simulation results. To eliminate randomness, five independent displacement cascade simulations are conducted, and the average result of the five cases is utilized for the statistical analysis of irradiation defects. In each displacement cascade simulation, atomic velocities are randomly altered, while keeping the temperature of the ensemble unchanged.

It is worth noting that the MD simulations are conducted under the extremely short time scale and the thermal equilibrium conditions, whereas the actual radiation damage involves the non-equilibrium state and subsequent annealing process. These processes encompass the long-distance diffusion, recombination, and clustering of defects. Hence, the comprehensive understanding of the overall radiation damage, especially mesoscale defect aggregation and cluster formation, would not be fully addressed using MD simulations. For example, the annealing stage is explored using kinetic Monte Carlo method (Li et al., 2023e, 2022c) and rate theory (Cooper et al., 2021; Xiong et al., 2023). Despite these limitations, MD simulations of displacement cascades remain crucial because the irradiation defects produced by displacement cascades serve as the foundation for the defect evolution in subsequent annealing process. Thus, the present work primarily focuses on studying the primary irradiation events within the 10–20 ps displacement cascade stage using MD simulations.

3. Results

This section begins by presenting the atomic configurations of the GBs before cascade. Subsequently, the defect evolution during the collision cascade is comprehensively introduced, including the atomic details and the statistics of defect numbers. In the third part, the correlation between the GB properties (GB misorientation, GB excess energy and GB excess volume) and irradiation damage characteristics (peak defects, surviving defects and defect absorption rate at GBs) are systematically analyzed.

3.1. Atomic structure of the GB

The atomic details of the GB structures in Ni and NiCoCr before the cascade collision simulation are illustrated in Figs. 2 and 3, respectively. In pure Ni, GBs consist of periodic arrays of ordered structural units (Fig. 2), aligning with prior research findings (Bourasseau et al., 2022; Frolov et al., 2013a; Lu et al., 2022; Medlin et al., 2017; Pan and Rupert, 2016; Zhu et al., 2017). Twin boundaries manifest as monolayer hexagonal-close-packed (HCP) atomic planes. Notably, the 210b, 310b, and 750b GBs comprise the typical normal-kite unit (Bourasseau et al., 2022; Frolov et al., 2013a; Medlin et al., 2017; Zhu et al., 2017), while the 331a and 331b exhibit the flat-kite unit. Other GBs, such as 210a (shrink-kite unit), 310a (split-kite unit), 650a, 650b, and 750a (distorted-kite units), as well as 113a and 113b (diamond units), demonstrate distinct structural variations (Frolov et al., 2013a; Pan and Rupert, 2016; Zhu

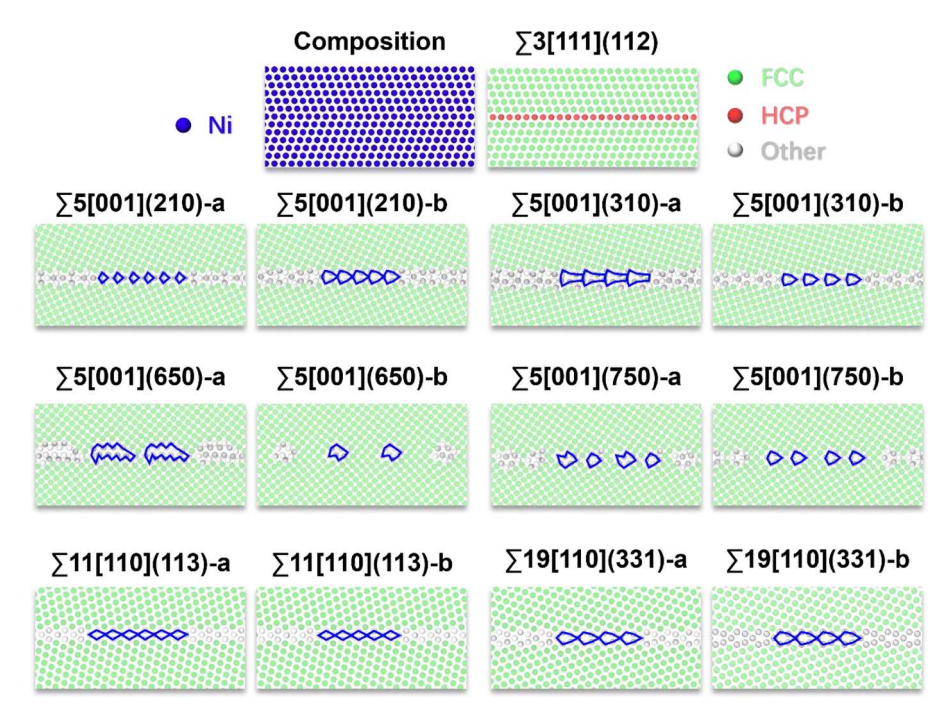


Fig. 2. Composition map and GB structures in pure Ni bicrystals. The atomic details of the structure units of GBs are outlined by blue lines.

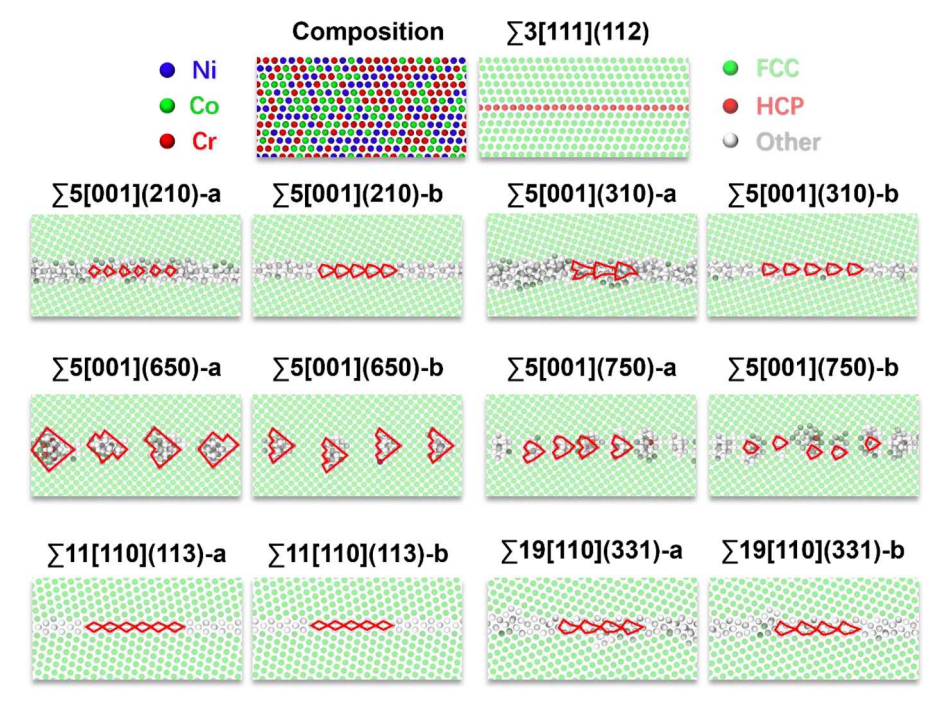


Fig. 3. Composition map and GB structures of NiCoCr bicrystals. The atomic details of the structure units of GBs are outlined by red lines.

et al., 2017). It's worth noting that while multiple GBs share a kite-like shape in their structural units, minor differences persist in the atomic structure among GBs with varying misorientation and tilt axes.

In MPEAs, the GB structures undergo distortion and partially disorder (Fig. 3) (Tan et al., 2021; Zhou et al., 2016a). The structures

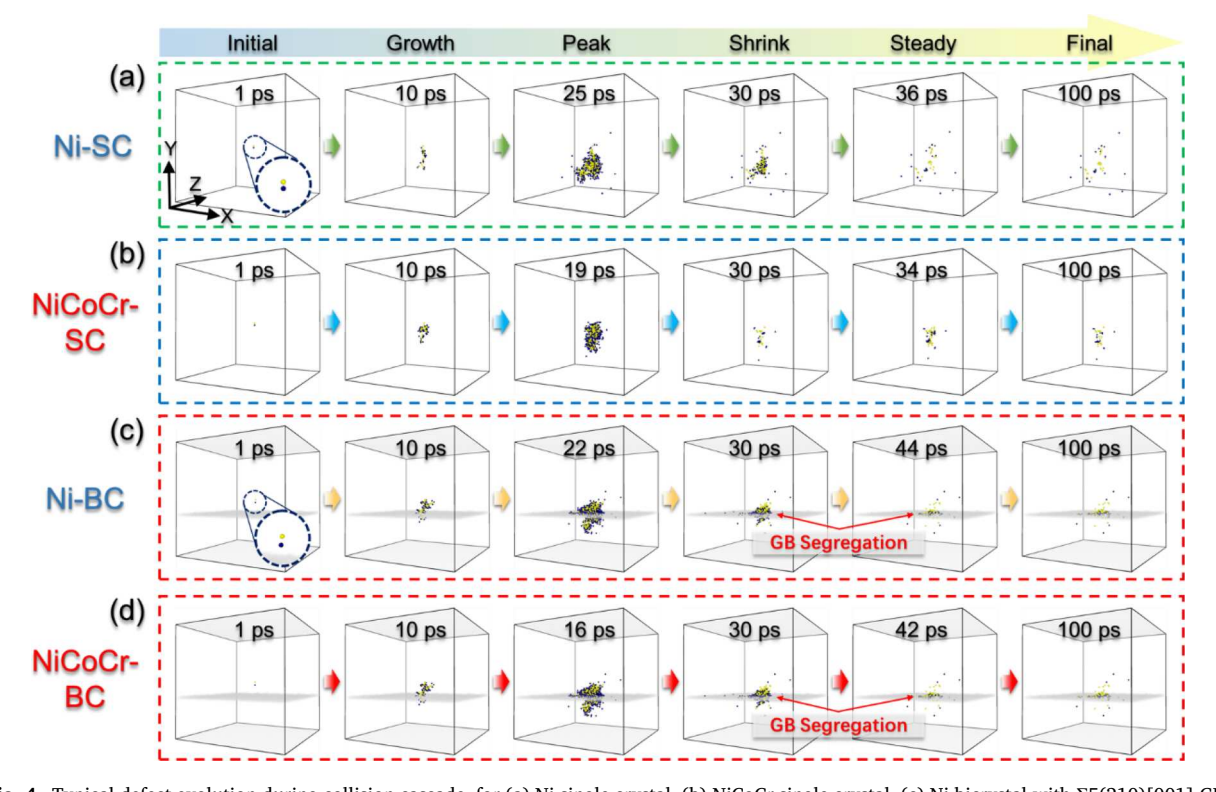


Fig. 4. Typical defect evolution during collision cascade, for (a) Ni single crystal, (b) NiCoCr single crystal, (c) Ni bicrystal with Σ 5(210)[001] GB, and (d) NiCoCr bicrystal with Σ 5(210)[001] GB.

of some GBs are stable and almost unchanged, including the twin boundary, 210b, 310b, 113a, and 113b GBs. For the 210a, 331a, and 331b GBs, the structures experience slight distortion, but the periodic arrays' structural units remain discernible. Conversely, the 310a, 650a, 650b, 750a, and 750b GBs exhibit severe structural distortion, with some units becoming entirely disordered. It is noteworthy that the structures of 650a, 650b, and 750a GBs exhibit the extended-kite feature, as reported in other pure metals (Zhu et al., 2017). This suggests that the steady-state GB structures differ among different systems for the same GB geometry parameters (tilt axis, misorientation, atomic density). This phenomenon also indicates an ordered GB phase transition induced by composition changes (Ma et al., 2012; Wang et al., 2011). For the 650b GB in NiCoCr, some structural units remain ordered, and others become disordered. The coexistence of ordered and disordered structures GBs results from specific boundary conditions (fixed atomic density at the GB) and a complex chemical environment. In cases where the atomic density at the GBs is variable, such as for the GBs in interconnected GBs network in polycrystalline materials, GBs in complex chemical environments may undergo globally ordered phase transitions akin to those in conventional alloys (Frolov et al., 2013b; Meiners et al., 2020; Wei et al., 2021).

3.2. Defect evolution of collision cascade

The progression of irradiation defects during the collision cascade is illustrated in Figs. 4 and 5. The cascade is delineated into six stages; initial, growth, peak, shrink, steady, and final stages (Lin et al., 2020; Shim et al., 2006). 1) Initial Stage; At the outset, the PKA is endowed with initial kinetic energy, striking the first atom and generating the initial vacancy-interstitial atom pair, commonly known as the Frenkel pair (FP). Throughout the cascade reaction, subsequent collisions lead to the production of additional FPs. Concurrently, some FPs annihilate due to the recombination of vacancies and interstitials. Consequently, the number of FP pairs is contingent upon the balance between production and annihilation events. 2) Growth Stage: Following PKA activation, the cascade reaction enters the growth stage. During this phase, the rate of FP production greatly surpasses the rate of annihilation, resulting in a rapid increase in the FP number and the expansion of the cascade-reaction impact area. 3) Peak Stage: Continuing the cascade reaction, the creation and annihilation rates for FPs progressively converge. Once dynamic equilibrium is reached between FP creation and annihilation, the number of FPs reaches its peak and the cascade reaches the commonly known thermal peak state. 4) Shrink Stage: Following the thermal peak of cascade, the annihilation rate of FPs surpasses the production rate, marking the onset of the shrink stage. As the kinetic energy of atoms at the cascade impact zone's periphery diminishes rapidly, the entire groups of FPs contract from the outer regions toward the center. If vacancies and interstitials are distant and lack the kinetic energy to approach each other, they persist within the alloy, evolving into stable surviving point defects. In samples featuring GBs, some point defects are drawn toward the GB, leading to defect segregation (Fig. 4(c, d)). It's noteworthy that defect segregation is more pronounced when the thermal peak area of the cascade collision coincides with the GB (Chen et al., 2023; Zhang et al., 2015a). This ideal phenomenon is likely to occur in nanocrystalline materials, it may be infrequent in coarsened grains. In coarsened-grained materials, a fraction of PKA may directly

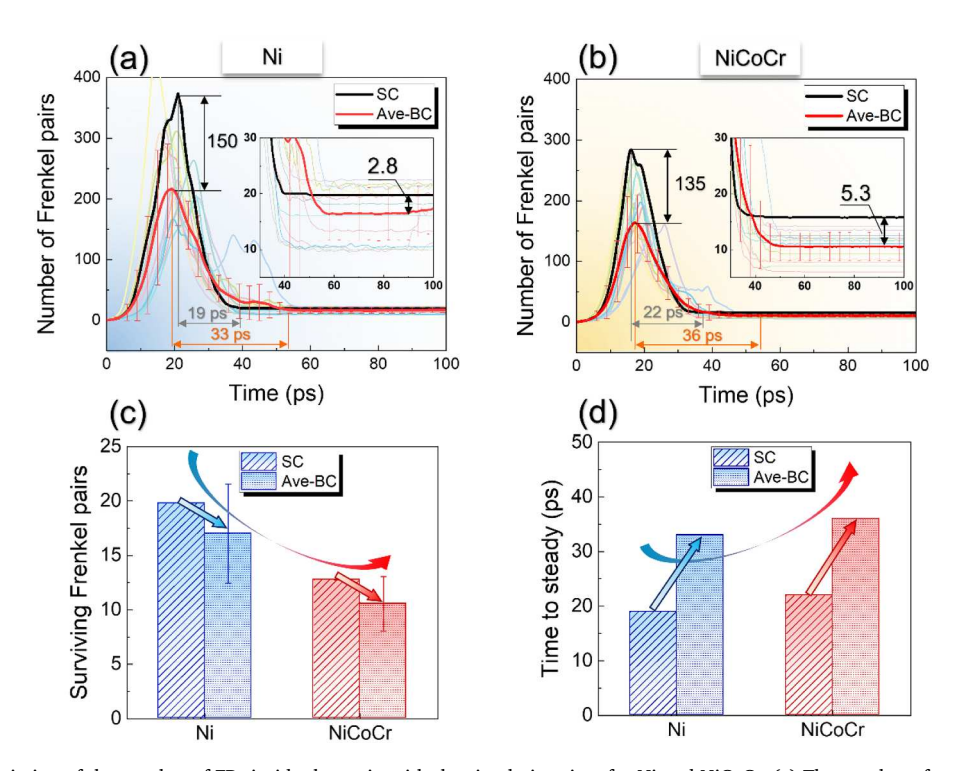


Fig. 5. (a, b) Variation of the number of FPs inside the grain with the simulation time for Ni and NiCoCr. (c) The number of surviving FPs in the single-crystal (SC) and bicrystal (BC) samples. (d) Total time taken for the cascade reaction to reach the stable stage from the peak stage.

interact with GBs, depleting defects near these GBs. Consequently, the concentration gradient induces long-range diffusion of defects within the grains, culminating in defect segregation at GBs. 5) Steady Stage: Once there are no more vacancies and interstitial atoms in the system that can approach each other, and no further defects annihilation occur, the collision cascade reaches a steady stage. 6) Final Stage: Subsequently, minor vacancies and interstitial atoms recombine under thermal activation. The number and distribution of defects in the final and stable states become nearly consistent.

The cascade stages outlined above are universal across various systems with distinct compositions and microstructures. However, the initiation moment and duration of each stage vary among different alloys, influencing the number and distribution of FPs in each stage. Fig. 5 illustrates the evolution of the number of surviving defects within the grain over the cascade time. The FP count consistently initiates from zero, undergoing a "zero-climb-peak-decline-stable-final" process, corresponding to the six stages illustrated in Fig. 4. Regarding the number of FPs, the peak FPs in the bicrystal model are notably lower than those in the single-crystal model, for both pure Ni and NiCoCr. This reduction is approximately 40–45 % (Fig. 5(a, b)), attributed to defect segregation to GBs (Fig. 4(c, d)). The average number of surviving FPs in the bicrystal model is also lower than that in the single-crystal model (refer to the enlarged images in Fig. 5(a, b)). Additionally, the surviving FPs in every NiCoCr bicrystal is less than that in the Ni bicrystal with the same GB type (Fig. 6(d)). These findings suggest that GBs generally mitigate radiation damage, aligning with experimental results indicating higher irradiation resistance in nanograined materials (El-Atwani et al., 2019; Hendy and Ponga, 2023; Wu et al., 2022).

The number of peak FPs (150 for BC model, 300 for SC model) and surviving FPs (11 for BC model, 17 for SC model) in NiCoCr is significantly lower than the peak FPs (210 for BC model, 380 for SC model) and surviving FPs (18 for BC model, 20 for SC model) in Ni. It's thereby suggested that NiCoCr exhibits higher resistance to irradiation damage. Moreover, the NiCoCr experiences a more pronounced reduction in the number of surviving FPs after the introduction of GBs: the average reduction is 5.3 for NiCoCr and 2.8 for Ni based on total 65 cascade simulations (Fig. 5(a, b)). The number of surviving FPs aligns with the levels observed in previous cascade simulations under 10 keV conditions (Chen et al., 2023; Wang et al., 2017). Furthermore, the relatively small data fluctuation of surviving FPs in NiCoCr, particularly evidenced in the enlarged images in Fig. 5(a, b), suggests a consistent resistance of the majority of NiCoCr GBs to irradiation damage. The GB resistance to irradiation damage is defined as the capacity of GBs to effectively mitigate both peak and surviving defects. This capacity is intricately linked to the efficient absorption or inhibition of defects by GBs, underscoring their pivotal role in reducing stable defects. Consequently, our findings indicate a general enhancement in GB resistance to irradiation damage in NiCoCr.

Concerning the time taken for each cascade stage, our primary focus is on the duration from the peak stage to the stable stage, as this stage determines the final state of surviving defects. As depicted in Fig. 5, the introduction of the GB into the model prolongs the time taken to reach the stable stage for both pure Ni and NiCoCr alloy. Furthermore, compared to pure Ni, the NiCoCr system, for both single-crystal and bicrystal models, exhibits a lengthier duration to achieve the stable state. Generally, the time required to reach the stable stage is inversely related to the energy dissipation capacity or thermal conductivity. A lengthier time to reach the stable stage

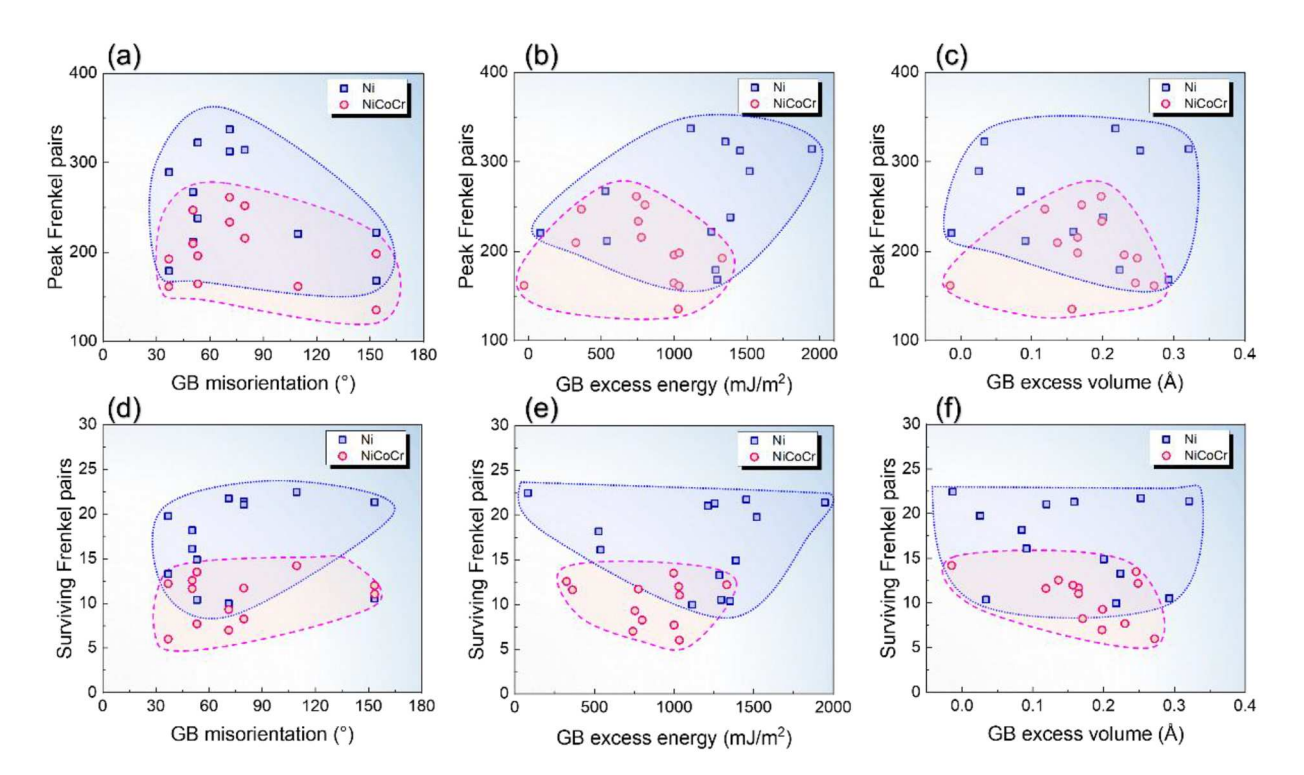


Fig. 6. Relationships between the number of peak FPs and (a) GB misorientation, (b) GB excess energy, and (c) GB excess volume. Relationships between the number of surviving FPs and (d) GB misorientation, (e) excess energy, and (f) excess volume.

suggests that radiation defects have more time for recombination, thereby reducing the number of surviving FPs. This deduction provides an explanation for the observed result that the irradiation damage in multi-principal-element/bicrystal systems is lower than that in unary/single-crystal systems. Previous studies have demonstrated that GBs can effectively scatter low-frequency phonons, thereby reducing thermal transport in crystalline materials (Fujii et al., 2020; Mohr et al., 2017). A recent study reports that the lower thermal conductivity of MPEAs facilitates the recombination of irradiation defects (Lin et al., 2020; Zhang et al., 2015b). Overall, these results suggest that the combined effects of GB and complex chemical environment in MPEAs significantly reduce thermal conductivity, thereby enhancing FP annihilation and reduce damage.

3.3. GB properties and collision-cascade defects characteristics

The influence of GBs on the cascade reaction has not been clarified because both the GB and cascade reaction are characterized by various parameters. Generally, the misorientation angle, θ , is used to describe the geometry of GB (Olmsted et al., 2009), and the excess energy and excess volume are used to represent the thermodynamics of GB (Fischer et al., 2019; Zheng et al., 2020); for collision cascade, the peak number and surviving number of FPs are mainly concerned.

Fig. 6 illustrates the relationship between GB properties and the number of peak/surviving FPs. Both the numbers of peak FPs and surviving FPs in NiCoCr are lower than that in pure Ni. Furthermore, for both Ni and NiCoCr systems, GBs with the close properties may correspond to huge difference of peak/surviving FPs. Previous studies that only concerned a limited number of GBs suggested that GBs with large misorientation, free energy, and excess volume can achieve lower irradiation damage. By analyzing a broad range of characteristic properties of GBs, our results indicate that the conclusions drawn from existing literature are somewhat contingent. Besides, there is no obvious connection between these GB properties and the numbers of peak FPs and surviving FPs in Fig. 6, indicating that GB properties do not directly influence the number of irradiation defects.

The impact of GBs on irradiation vacancies and interstitials varies due to the differing thermodynamic properties of these two types of point defects. Fig. 7(a–c) depict the relationship between GB properties and the number of surviving vacancies and interstitials. In both pure Ni and NiCoCr systems, the surviving interstitial atoms are less than the vacancies. The majority of interstitial atoms are absorbed by GBs, resulting in a high absorption rate of interstitial atoms. This trend is partially related to the lower migration energy and higher diffusion rate of interstitial atoms in alloys (Bai et al., 2010; Samaras et al., 2003; Smirnov, 2020; Takahashi and Hashimoto, 1993). Moreover, the number of surviving vacancies and interstitials in NiCoCr is consistently lower than that in pure Ni, indicating that the GB absorption abilities for both vacancies and interstitial atoms are enhanced in NiCoCr.

The defect absorption rate at GB is further calculated and presented in Fig. 7(d-f). In this context, the defect absorption rate, denoted as f_d , is defined as the ratio between the number of defects located at the GB, n_{def}^{GB} , and the total defects retained in the grain, n_{def} , i.e., $f_d = n_{def}^{GB}/n_{def} \times 100$ %. The defect absorption rate serves as a pivotal metric in understanding how effectively the GB

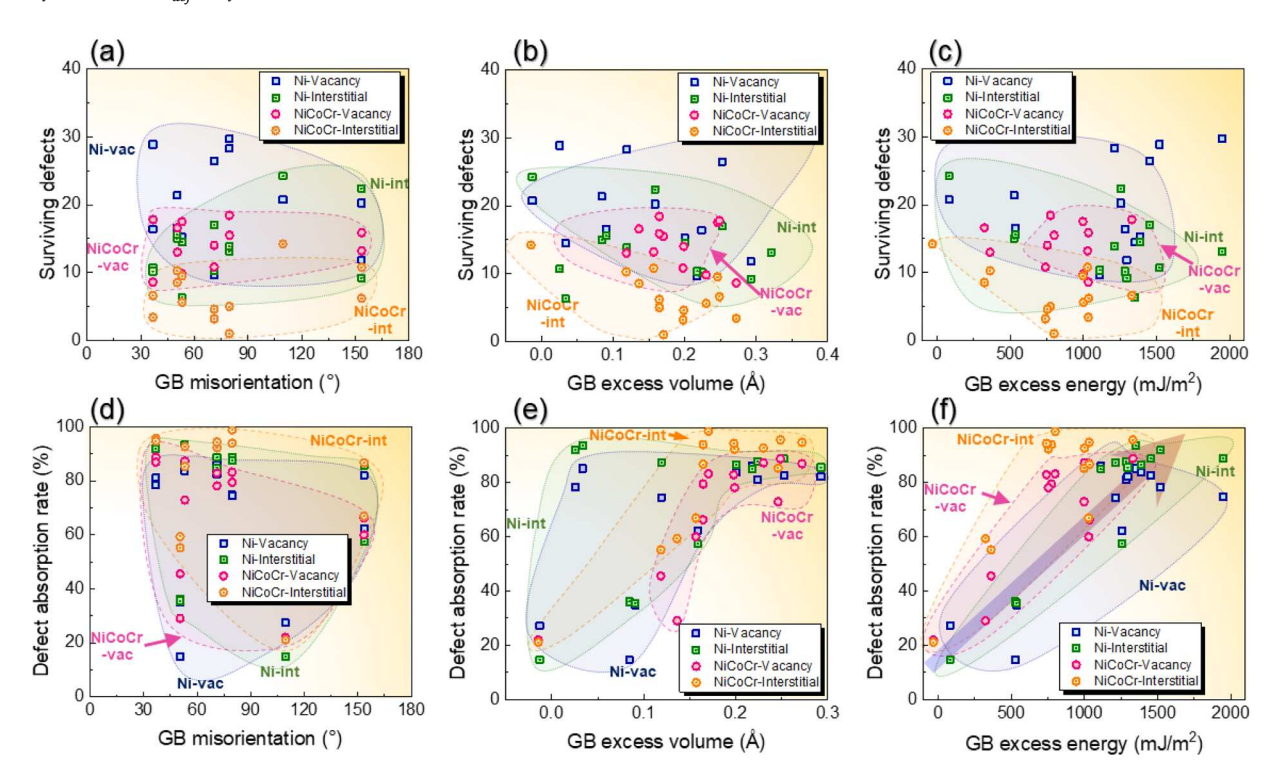


Fig. 7. Relationships between the number of surviving FPs and (a) GB misorientation, (b) GB excess volume, and (c) GB excess energy. Relationships between the defect absorption rate at GBs and (d) GB misorientation, (e) GB excess volume, and (c) GB excess energy.

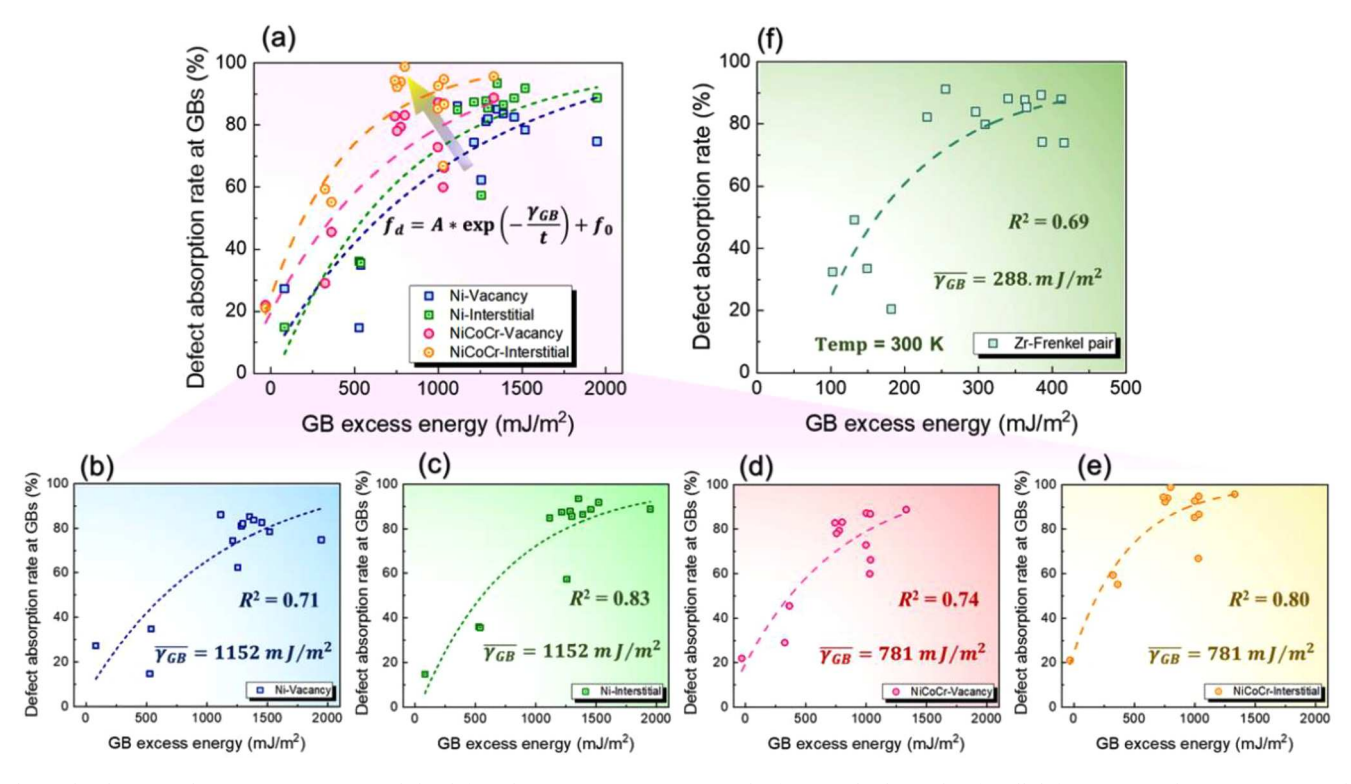


Fig. 8. Functional relationship between the GB excess energy and the defect absorption rate at GBs. (a) The functional relationship for all defects in Ni and NiCoCr systems. The expression for the relationship between the GB excess energy and the defect absorption rate is included. (b) The relationship for vacancies in Ni. (c) The relationship for interstitials in Ni. (d) The relationship for vacancies in NiCoCr. (e) The relationship for interstitials in NiCoCr. The average GB excess energy and the coefficient of determination (R-squared) for the fitting are given in (b)-(e). (f) Functional relationship between the GB excess energy and the defect absorption rate at GBs after the collision cascade in HCP Zr. The data is obtained from literature (Xu et al., 2024).

mitigates the impact of irradiation-induced defects within the material. The count of surviving defects, influenced directly by the defect absorption rate, provides crucial insights into the GB's ability to withstand irradiation damage. A higher defect absorption rate signifies a more robust defense mechanism at the GB, resulting in a greater reduction in the overall number of surviving defects. Consequently, an increase in the defect absorption rate not only indicates a more efficient absorption of defects at the GB but also signifies a notable enhancement in the GB resistance to irradiation damage.

Note that the GB experiences slight changes under the influence of collision cascade. As a result, statistics on defects at GBs may be inaccurate using the Wigner-Seitz method. However, the structural changes of the GB are limited to its central region, where the absorption density of defects is very high. Therefore, the additional defects contributed by the GB structural change are not expected to have a significant impact on the overall defect number at the GB. Such inaccuracy is further faded by performing multiple independent cascade simulations. Additionally, the Wigner-Seitz method remains widely accepted for analyzing irradiation defects at GBs (Bai et al., 2010; Li et al., 2023c; Zhang et al., 2015a), and the resulting conclusions align well with common knowledge.

From Fig. 7(d–f), it can be observed that the defect absorption rate is not clearly correlated with the GB misorientation and GB excess volume. However, the defect absorption rate roughly increases with the rise in GB excess energy (Fig. 7(f)). This trend suggests that GB excess energy may be a crucial factor influencing the resistance of GBs to irradiation damage. Accordingly, it is logical to deduce that the anti-irradiation ability of the a-GBs and b-GBs, characterized by the same misorientation but different atomic density, is primarily controlled by their GB excess energy, i.e., the GB with high energy tends to exhibit the high irradiation resistance. Due to the excess energy of a-GBs is not always higher or lower than that of b-GBs (Table 1), there is no consistent pattern regarding the strength of their anti-irradiation ability. In addition, Fig. 7(f) also show that the absorption of GBs in NiCoCr is more pronounced than in Ni, and the absorption rate of interstitials is higher than that of vacancies. These results align with the observations in Fig. 7(a–c), where fewer defects survive in NiCoCr, and more interstitial atoms are retained in the grain.

4. Discussion

Irradiation damage is closely linked to the number of surviving defects, and this number is diminished by an enhanced defect absorption rate at GBs. In the following sections, the underlying correlation between the defect absorption rate and GB energetic states is first discussed, revealing that GB excess energy and defect segregation energy are critical properties influencing the defect absorption rate. Subsequently, the key GB property that contributes to the improved defect absorption rate at GBs in NiCoCr is unveiled. The essential role of GB disorder and GB entropy in influencing GB sink strength is then discussed based on thermodynamic analysis. Finally, the impact of specific elements in NiCoCr is also examined.

4.1. Relationship between GB excess energy and defect absorption rate at GBs

The results in Fig. 7(f) indicate a positive correlation between the defect absorption rate at GB and GB excess energy. We independently analyze the mathematical relationship between the absorption rate of vacancies and interstitials corresponding to different GB excess energies (Fig. 8). Surprisingly, there is a concise exponent relationship between the defect absorption rate and GB excess energy, representing as:

$$f_d = A \cdot exp\left(-\frac{\gamma_{GB}}{t}\right) + f_0 \tag{2}$$

where f_d is the defect absorption rate at GB, γ_{GB} is the GB excess energy, f_0 is the intrinsic defect absorption rate that is sensitive to the material system, t is a parameter controlling the sensitivity of the defect absorption rate on the GB excess energy, A is the prefactor. The corresponding fitting parameters are given in Table 2. This functional relationship proves to be applicable across different systems and different types of defects, suggesting a degree of universality. Here, it is worth to note that the exponent formation of the defect absorption rate - GB energy relationship is informed by the well-established thermodynamic principles involving GBs, such as the exponent relationship between grain growth rate and grain growth activation energy (Aust, 1969; Swalin and Rice, 1963), the relationship between GB diffusion coefficient with diffusion activation energy (Frolov et al., 2013a; Schweizer et al., 2023; Suzuki and Mishin, 2005), and the equilibrium concentration of GB solute (Raabe et al., 2014; Svoboda et al., 2006). This consistency implies a shared thermodynamic nature among these relationships.

Given that Eq. (2) is informed by the traditional thermodynamic principles with exponent format, it is logical to deduce that the parameter t in Eq. (2) is positively related to the temperature T, i.e., $t \propto T$. But the exact mathematic relationship between parameter t and temperature T cannot be obtained based on the current cascade simulation data that merely concern one temperature. A recent MD work for the 300 K collision cascade in T bicrystal also notice that the trend of T because the T because T is analyzing their data, we also find an exponent relationship between the T because T is logical to deduce that the parameter T cannot be obtained based on the current cascade simulation data that merely concern one temperature. A recent T work for the 300 K collision cascade in T bicrystal also notice that the trend of T between the T because T is an alyzing their data, we also find an exponent relationship between the T because T is an alyzing their data.

Table 2 Fitting parameters of Eq. (2) through the data presented in Fig. 8.

	Ni-vacancy	Ni-interstitial	NiCoCr-vacancy	NiCoCr-interstitial	Zr-Frenkel pair
f_0	103.88	100.00	106.06	100.00	94.20
A	-84.33	-75.55	-100.90	-104.54	-146.44
$t~(\mathrm{mJ}/\mathrm{m}^2)$	818.40	469.90	1103.24	753.84	135.20

absorption rate (Fig. 8(f)), akin to the Eq. (2) revealed by the present work. This finding strongly supports the university of Eq. (2) among different metal systems and various temperature. Thus, while derived from low-temperature cascade simulations, the obtained relationship holds promise for validity at elevated temperatures as well.

Leveraging the exponent relationship elucidated above, it becomes apparent that the sensitivity of the defect absorption rate to GB energy is more pronounced when the GB energy is relatively low. This sensitivity implies a substantial divergence in the anti-irradiation ability among low-energy GBs within a specific polycrystalline sample. On the contrary, for high-energy GBs ($\gamma_{GB} > 1000 \text{ mJ/m}^2$), the variance in defect absorption rate becomes negligible. In practical materials, high-energy GBs often dominate with similar structures, resulting in comparable resistance to irradiation damage across most GBs. Consequently, optimizing the irradiation resistance of a given system becomes feasible primarily by increasing GB density. Current alloying techniques propose methods to lower GB energy, usually aiming to enhance high-temperature stability and strength (Lu et al., 2009; Prithiv et al., 2018; Zhou et al., 2018). These alloys can potentially fine-tune GB energy using the derived mathematical expressions, offering a pathway for a synergistic optimization of high-temperature stability, strength, and irradiation resistance in the alloy.

Referring to Fig. 8(a), the defect absorption rate follows the order: interstitials in NiCoCr > vacancies in NiCoCr > interstitials in Ni > vacancies in Ni. This quantitatively validates the superior resistance of NiCoCr alloy to irradiation damage compared to pure Ni, particularly regarding irradiation-induced interstitials. The exponent relationship suggests that high-energy GBs exhibit a higher absorption rate for defects. However, even though the average GB excess energy of NiCoCr ($\gamma_{GB}^{NiCoCr} = 781 \text{ mJ/m}^2$) is lower than that of pure Ni ($\gamma_{GB}^{Ni} = 1152 \text{ mJ/m}^2$), the defect absorption rate in NiCoCr remains relatively high. This indicates that GB excess energy might not be the sole determinant of the defect absorption rate. To unravel this discrepancy, the subsequent section independently delves into the segregation energy of vacancies and interstitials at GBs.

The aforementioned discussion highlights the potential to enhance GB sink strength by elevating GB energy, offering a clear strategy for mitigating irradiation damage in polycrystalline materials. However, increasing GB energy comes at the cost of diminished thermal stability of GBs (Fu et al., 2022; Kusama et al., 2017; Zhang et al., 2022a). The interplay between GB sink strength and GB stability emerges as a pivotal challenge in GB engineering for irradiation-resistant materials. An effective approach to navigate this dilemma involves boosting the kinetic stability of GBs by restraining GB motion. In MPEAs, lattice distortion induces heterogeneous lattice strain at the atomic scale, effectively impeding the motion of crystal defects like dislocations (Chen et al., 2020a; Li et al., 2020, 2023d). This lattice strain also creates sporadic high-stress regions that act as pinning points to hinder GB motion (Li et al., 2023b; Luo and Zhou, 2023), thereby enhancing the kinetic stability of GBs. Consequently, the competition between GB sink strength and GB stability is partially alleviated and weakened in MPEAs.

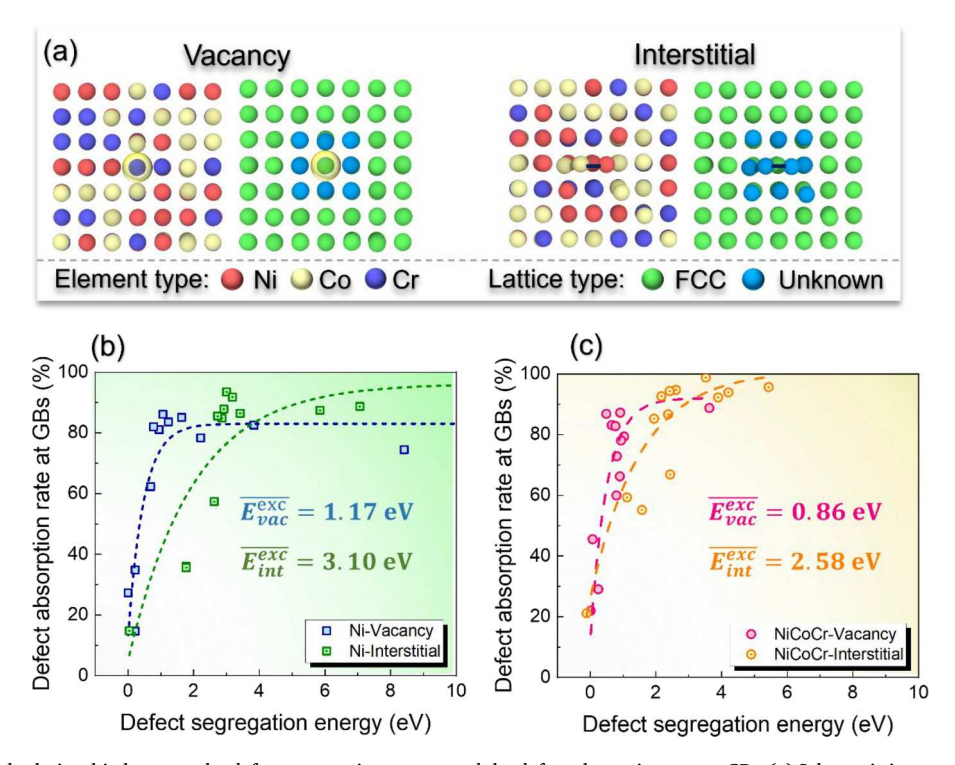


Fig. 9. Functional relationship between the defect segregation energy and the defect absorption rate at GBs. (a) Schematic image of the vacancy and interstitial in NiCoCr. (b) Relationship between the defect segregation energy and the defect absorption rate in pure Ni. (c) Relationship between the defect segregation energy and the defect absorption rate in NiCoCr.

4.2. Relationship between defect segregation energy and defect absorption rate

According to the thermodynamic theory, the driven force for defects segregating to the GB is controlled by the defect segregation energy, i.e., the energy difference between the defect formed in the grain and in the GB. The defect segregation energy is given by:

$$E_{def}^{seg} = E_{def}^{SC} - E_{def}^{BC} \tag{3}$$

where E_{def}^{seg} is the defect segregation energy. E_{def}^{SC} and E_{def}^{BC} are the formation energies of the defects in grain and GB, respectively. For a system composed of N atoms, the energy required for forming a vacancy at a lattice site i, E_{vac}^{for} , is equal to the difference in energy between this system and a vacancy-free system consisting of N-1 atoms (Bai et al., 2010; Li et al., 2023e; Zheng et al., 2023), i.e.,

$$E_{vac}^{for} = E_{vac} - E_{novac} + \mu_i \tag{4}$$

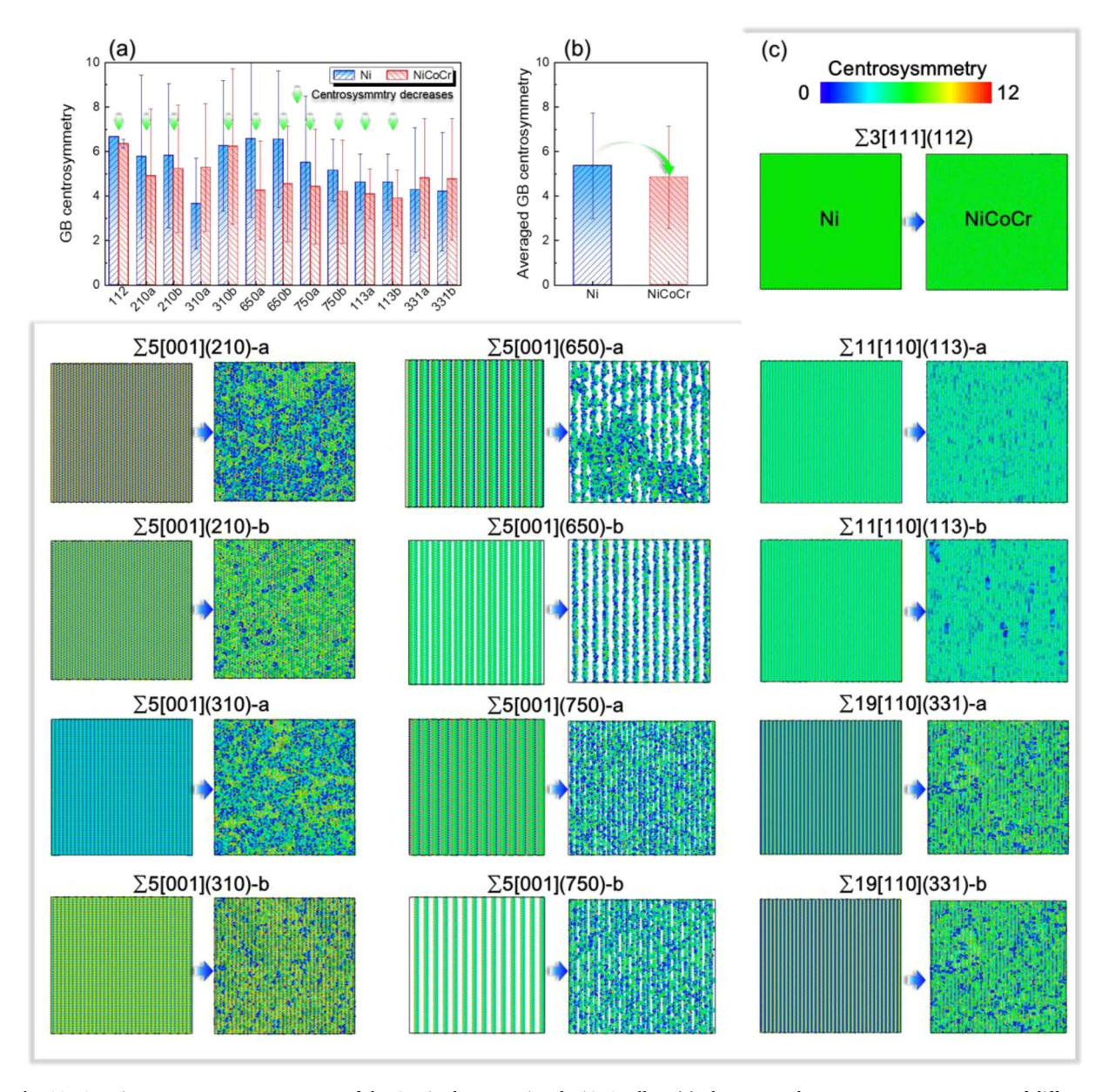


Fig. 10. Atomic centrosymmetry parameter of the GBs in the pure Ni and NiCoCr alloy. (a) The averaged centrosymmetry parameter of different GBs. The green arrow marks the case where the centrosymmetry parameter of NiCoCr is lower than that of Ni. (b) The averaged GB atomic centrosymmetry of all GBs in Ni and NiCoCr. (c) Distribution of the atomic centrosymmetry parameter on different GBs. The atoms are colored according to their centrosymmetry parameter.

where E_{novac} and E_{vac} are the potential energies of the vacancy-free system and the system containing one vacancy. μ_i is the potential energy of the atom originally located at the lattice site i. For the vacancy in GB, μ_i is the average potential energy of all atoms in the GB that have the same element type as atom i.

Similarly, the interstitial atom formation energy, E_{int}^{for} , is given by:

$$E_{int}^{for} = E_{int} - E_{noint} - \mu_i \tag{5}$$

where E_{noint} and E_{int} are the potential energies of the system before and after inserting an interstitial atom.

Fig. 9 illustrates the relationship between defect segregation energy and defect absorption rate at GBs. Notably, there are exponent relationships between the defect absorption rate and defect segregation energy for both systems and types of defects, aligning with the findings in Fig. 8. This reaffirms that the GB energetic state (GB excess energy or defect segregation energy) governs the resistance of GBs to irradiation damage. In Fig. 9, it is evident that the defect segregation energy in NiCoCr is lower than that in pure Ni, mirroring the trend observed in GB excess energy. The average vacancy segregation energy in NiCoCr, $E_{vac-NiCoCr}^{seg} = 0.86$ eV, is lower than that in Ni, $E_{vac-Ni}^{seg} = 1.17$ eV; similarly, the average interstitial segregation energy in NiCoCr, $E_{int-NiCoCr}^{seg} = 2.58$ eV, is lower than that in Ni, $E_{int-Ni}^{seg} = 3.10$ eV.

Interesting, while both interstitial and vacancy segregation energies in NiCoCr decrease, the reduction in interstitial segregation energy is more pronounced. Specifically, the interstitial segregation energy experiences a greater reduction of 0.52 eV, surpassing the reduction observed in vacancy segregation energy of 0.31 eV. The uneven reduction in defect segregation energies reduces the gap between interstitial and vacancy segregation energies. In NiCoCr, the interstitial-vacancy segregation energy difference is 1.72 eV, 11 % lower than the 1.93 eV difference in Ni. This suggests a higher fraction of interstitial atoms stays within the grain interior, facilitating recombination between interstitials and vacancies. With more defects consumed within the grains, the proportion of defects at GBs increases. Ultimately, this results in an increased defect absorption rate at GBs. In short, the enhanced defect absorption rate in NiCoCr stems from the reduced difference between interstitial and vacancy segregation energies.

It is noteworthy that the average GB excess energy and defect segregation energy exhibit a similar relationship with the defect absorption rate at GBs, hinting at an inherent connection between them. From a thermodynamic perspective, the segregation of defects consumes GB excess energy and reduces the residual defect energy of the grain, leading to an overall reduction in the system's internal energy. Concurrently, the final number and fraction of irradiation defects are influenced by the difference between interstitial and vacancy segregation energy. A reduced difference implies that the numbers of interstitials and vacancies within the grain are comparable, facilitating defect recombination and, consequently, improving the defect absorption rate at the GB. Therefore, the ultimate conclusion is that the enhanced defect absorption rate at the GB can be attributed to the overall increase in GB energetic state (GB excess energy and defect segregation energy) and the biased reduction in interstitial segregation energy.

4.3. Influence of GB disorder

The atomic-level elemental heterogeneity is a core characteristic of MPEAs, significantly altering the configuration and activity of microstructures (Lee et al., 2020, 2018; Lu et al., 2016; Tandoc et al., 2023; Wang et al., 2020; Zhang et al., 2015b). Local lattice disorder causes atomic positions to deviate from ideal lattice sites, reducing the symmetry of the lattice. This degree of lattice disorder can be represented using the change in lattice symmetry (Kelchner et al., 1998). Fig. 10 depicts the distribution and statistical characteristics of the centrosymmetry parameter of GB atoms. As the GBs in pure Ni are composed of ordered structural units (Fig. 2), the distribution of atomic centrosymmetry parameters exhibits a periodic mode or uniform character (Fig. 10(c)). In contrast, for NiCoCr, a dramatic fluctuation in atomic centrosymmetry parameters is observed, diverging from the ordered feature in pure Ni. The averaged atomic centrosymmetry parameters for all GB are independently calculated, demonstrating that the lattice symmetry of most GBs in NiCoCr deviates from that in pure Ni (Fig. 10(a)), and the averaged lattice symmetry of the NiCoCr GBs is also distinct (Fig. 10

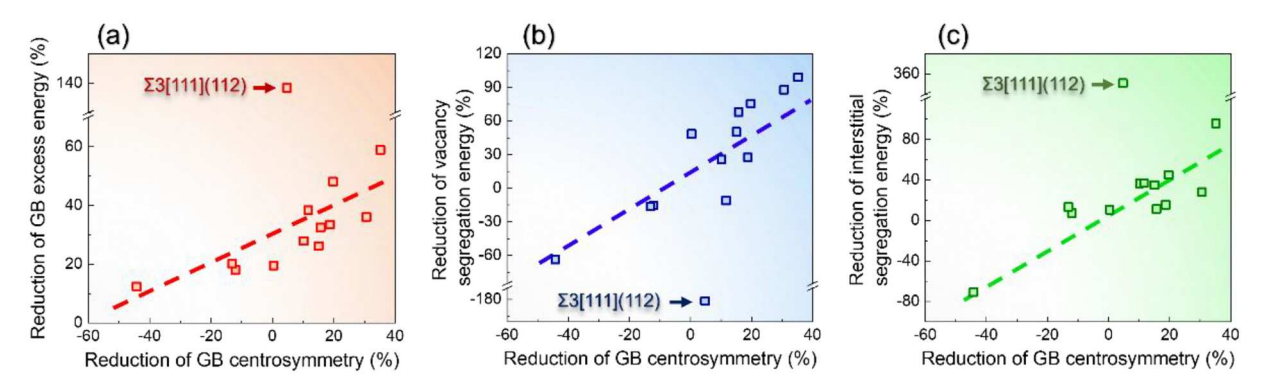


Fig. 11. Relationship between the reduction of averaged atomic centrosymmetry parameter of GBs and (a) the reduction of GB excess energy, (b) the reduction of vacancy segregation energy, and (c) the reduction of interstitial segregation energy.

(b)). These results illustrate that the atomic-level elemental heterogeneity significantly alters the lattice symmetry of GBs in MPEAs. To quantify the influence of lattice disorder on the key GB properties that control the GB resistance to irradiation damage, the relationships between the GB atomic centrosymmetry parameter and the GB excess energy and segregation energy are analyzed. Here, the reduction of the GB property, C_{GB}^{dif} , is calculated by:

$$C_{GB}^{dif} = \frac{C_{GB}^{Ni} - C_{GB}^{NiCoCr}}{C_{GB}^{Ni}} \times 100 \%$$
 (6)

where C_{GB}^{Ni} and C_{GB}^{NiCoCr} represent the considered GB property, which can be the GB atomic centrosymmetry, GB excess energy and GB segregation energy. It's worth noting that the change in the GB atomic centrosymmetry reflects the degree of local lattice disorder in the distorted GB compared to the ordered GB. Fig. 11 illustrates the relationship between the GB atomic centrosymmetry parameter and the GB excess energy and defect segregation energy. Surprisingly, for most GBs, except for the $\Sigma 3[111](112)$ GB, the change in the atomic centrosymmetry parameter is linearly related to the reduction in GB excess energy and defect segregation energy. These results reveal that the decreased defect segregation energy is caused by the GB disordering in NiCoCr.

The uniqueness of the $\Sigma 3[111](112)$ GB arises from its high atomic-density structure and inherently low energetic state. The GB excess energy of the $\Sigma 3[111](112)$ GB is 82 mJ/m^2 in Ni and -31 mJ/m^2 , significantly lower than the average excess energy of other GBs (1240 mJ/m² in Ni and 781 mJ/m^2 in NiCoCr). In this context, even a slight change in the energy value leads to a substantial proportionate energy change. The reason for the low GB segregation energy of $\Sigma 3[111](112)$ GB is similar. Additionally, it's noteworthy that the vacancy segregation energy in the $\Sigma 3[111](112)$ GB is much lower than that of other GBs, while the interstitial segregation energy is much higher than that of other GBs. This is attributed to the $\Sigma 3[111](112)$ GB being composed of a single-layer of atoms with a highly dense structure, making it challenging to embed an atom, while relatively easier to remove an atom.

4.4. The essential role of GB entropy

According to the thermodynamic theory, the lattice-disorder-induced change of the GB energetic state inherently derives from the change of the enthalpy and entropy of the GB (Ragone, 1995; Swalin and Rice, 1963). Here, considering a GB structure unit composed with N lattice sites. When the GB unit is disorder, there are still $n_1 \leq N$ lattice sites stay at the normal position, while $n_2 \leq N - n_1$ sites deviate from the normal position. The order degree of GB can be defined as $\varphi = n_1/N$. Then the change of GB energy, ΔG_{dis} , due to the lattice disorder is given by:

$$\Delta G_{dis} = \Delta H_{dis} - T \cdot \Delta S_{dis}$$
 (7)

where ΔH_{dis} and ΔS_{dis} are the change of GB enthalpy and entropy, T is the current temperature. When one lattice site of the GB unit becomes disordered, the enthalpy change is ε_{dis} . In this case, the enthalpy change is positively related to the number of disorder site n_2 and can be written by:

$$\Delta H_{dis} = n_2 \cdot \varepsilon_{dis}$$
 (8)

Since we only care about the entropy change caused by changes of GB structure, it is assumed that there is only one element type for GB atoms. The structural entropy of the GB unit is determined by the number of configurations arranged by the normal and disorder sites:

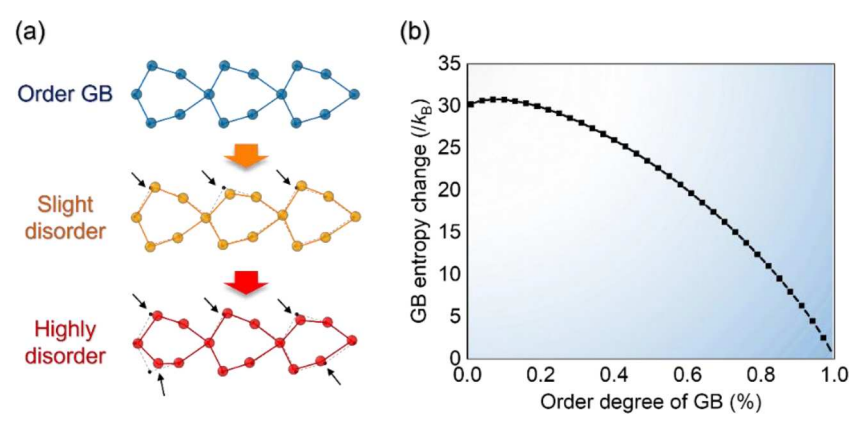


Fig. 12. Relationship between the GB disorder and GB entropy. (a) Schematic images of the GB structure units with different order degree. The black dots and dash lines represent the ideal lattice sites and configuration of the GB unit, respectively. The large spheres and solid lines are the current lattice sites and configuration of the GB unit, respectively. The black arrows mark the highly disorder sites. (b) Variation of the GB entropy change ΔS_{dis} with the order degree of GB φ . Assuming N=12 because the lattice structure of grain is face-cubic-center. Note that the trend in figure (b) is not sensitive to the specific value of N.

$$S_{dis} = k_B \ln \left(\frac{N!}{n_1! \cdot n_2!} \right) \tag{9}$$

where k_B is the Boltzmann constant. The entropy change is given by:

$$\Delta S_{dis} = k_B \ln \left(\frac{N!}{n_1! \cdot n_2!} \right) - k_B \ln \left(\frac{N!}{n_1(\varphi = 1)!} \right)$$

$$\tag{10}$$

Based on Stirling approximation $ln(a!) \approx aln(a) - a$, we get:

$$\Delta S_{dis} = k_R N (\ln N - \varphi \ln(N\varphi) - \ln(1 - \varphi) + \varphi \ln(1 - \varphi)) \tag{11}$$

Lastly, the impact of lattice disorder on the change in GB energy can be scrutinized using the above functions. In conventional crystalline materials, the enthalpy change associated with a disordered structure is typically positive, contributing to an increase in the enthalpy term ΔH_{dis} and subsequently increasing the GB energy. This is in apparent contradiction with the observed reduction in the GB energetic state of NiCoCr, as illustrated in Fig. 11. This incongruity suggests that entropy change may play a significant role in diminishing the GB energetic state. Fig. 12 illustrates the entropy change ΔS_{dis} for varying degrees of GB order φ . The positive values of ΔS_{dis} increase as the GB order degree decreases. This implies that GB disorder amplifies ΔS_{dis} , leading to a reduction in GB energy - an observation consistent with the diminished GB energetic state of NiCoCr. As enthalpy change tends to increase GB energy, these findings underscore the predominant role of entropy change in shaping the energetic state of GBs of NiCoCr.

4.4. Influence of specific elements

During the collision cascade, the high-throughput flow of point defects is accompanied by the spatial transport of atoms, leading to the redistribution of elements and consequent changes in the chemical environment, which in turn affect irradiation damage. To unveil the impact of the complex chemical environment on irradiation defects in NiCoCr, the composition of residual defects in the NiCoCr models is analyzed. In Fig. 13, it is observed that the residual vacancy group is generally encompassed by the interstitial atom group, due to the faster movement of interstitial atoms compared to vacancies in alloys (Chen et al., 2023; Hendy and Ponga, 2023; Takahashi and Hashimoto, 1993).

The element type of irradiation defects varies, and the element fraction is sensitive to the composition and GB structure (Manna and Pal, 2023; Zhao et al., 2023; Zhao et al., 2023). Here, the element type of a vacancy denotes the initial element of the corresponding

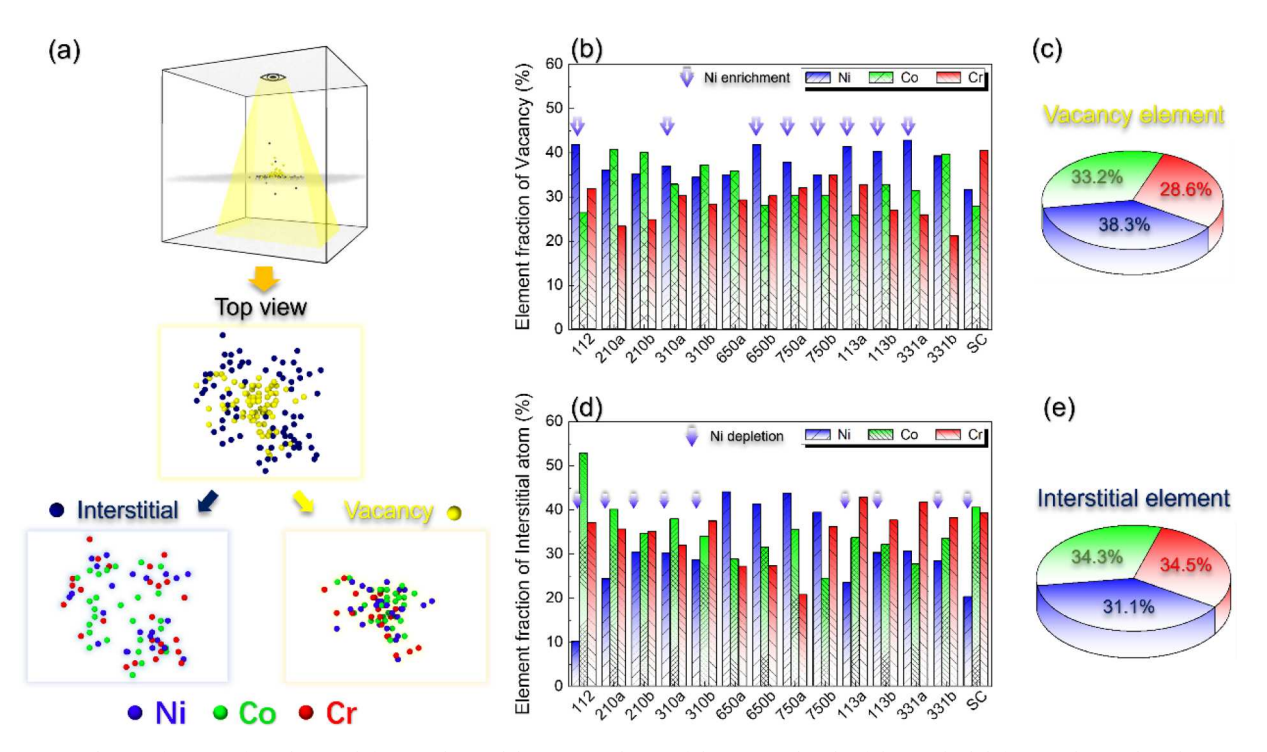


Fig. 13. Element fraction of irradiation defects in the model. (a) Typical case of the atomic details of the residual defects in the irradiated NiCoCr bicrystal. The distribution of vacancies and interstitial atoms, as well as the element type of these point defects, is presented. (b) The element fraction of the residual vacancies in the models with different GBs. (c) The average element fraction of the residual vacancies in all models. (d) The element fraction of the residual interstitial atoms in the models with different GBs. (e) The average element fraction of the residual interstitial atoms in all models.

atom originally located at the lattice site of the vacancy. Fig. 13(b–e) present the element fraction of the residual vacancies and interstitials in different models. Among the fourteen models, the vacancies in eight models are predominantly enriched with the Ni element (Ni enrichment), while the interstitials in nine models exhibit a relatively low Ni content (Ni depletion). The average fraction across all models also reflects a similar trend: the ordering of the element fraction for residual vacancies is $38.3 \,\%$ Ni $> 33.2 \,\%$ Co $> 28.6 \,\%$ Cr (Fig. 13(c)), and for interstitials, it is $31.1 \,\%$ Ni $< 34.3 \,\%$ Co $< 34.5 \,\%$ Cr (Fig. 13(e)). Recent experiments on the NiCoCrFe MPEA reveal that ion irradiation induces atomic-level segregation of Ni around the mono-vacancy-type damage at early stages of irradiation damage (Tuomisto et al., 2020). This suggests that Ni enrichment at irradiation-induced vacancies is a prevalent phenomenon in NiCoCr-based MPEAs.

To elucidate the influence of specific elements on GB resistance to irradiation damage, the element fractions of irradiation defects in the grain and GB are independently analyzed. As depicted in Fig. 14, both the surviving defects in the grain and the segregated defects in the GB commonly exhibit Ni-enriched vacancies and Ni-depleted interstitials. Notably, this Ni enrichment in vacancies and Ni depletion in interstitial atoms are more prominent for the surviving defects in the grain. Specifically, ten models show Ni-enriched surviving vacancies, whereas Ni-enriched segregated vacancies are observed in only nine models. Similarly, thirteen models exhibit Ni-depleted surviving interstitial atoms, while Ni-depleted interstitial atoms are observed in ten models. Fig. 14(c, f) present the average element fraction of all defects in the grain and GB, respectively. The surviving vacancies in the grain are enriched with Ni (38.6 % Ni > 31.9 % Co > 29.5 % Cr), and the depletion of Ni is more pronounced for the surviving interstitials (19.2 % Ni < 40.1 % Co < 40.7 % Cr).

It is essential to note that while the element type of segregated vacancies in the GB is still dominated by Ni (39.0 % Ni > 34.5 % Co > 26.5 % Cr), the Ni fraction of segregated interstitials is not the lowest (32.0 % Cr < 32.5 % Ni < 35.6 % Co). This observation is particularly noteworthy when considering the Ni depletion for the surviving interstitials, which is enhanced compared to the total interstitials in Fig. 13(e). It is reasonable to deduce that a substantial fraction of surviving Ni interstitials migrates into the GB. Simultaneously, the enrichment of Ni interstitials on GBs comes at the expense of Cr interstitials, resulting in the depletion of Cr interstitials in the irradiated GBs (Fig. 14(f)).

In traditional dilute alloys, such as Fe-Cr, Fe-Cr-Ni, and Fe-Cr-Mn, the migration of irradiation defects, especially interstitial atoms, towards the GBs leads to the enrichment of Ni and depletion of Cr on GBs (Takahashi and Hashimoto, 1993; Wharry and Was, 2014). This irradiation-induced redistribution of elements is typically attributed to the inverse Kirkendall effect (Marwick and Clark, 1989; Marwick and Piller, 1977) and the solute drag effect (Allen et al., 1998). The combination of these phenomena results in the retention of the low-diffusivity Ni element on GBs, while the high-diffusivity Cr element migrates away from GBs. Recent experiments also observed Ni enrichment and Cr depletion on GBs in the irradiated FeNiMnCr MPEA (Kumar et al., 2016) and Al0.1CoCrFeNi (Yang et al., 2018). Utilizing Positron annihilation spectroscopy and first-principles calculations, studies unveiled that atomic segregation of Ni occurs at very early stages of radiation damage in 2–4 element NiCoFeCr MPEAs (Tuomisto et al., 2020). These findings support the notion that irradiation-induced element redistribution in MPEAs is influenced by the diffusivity of specific elements.

Experiments and simulations have demonstrated that in NiCoCr-based MPEAs, such as CoCrFeNiMn and CoCrFeNi, the diffusivity of Cr is higher than that of Ni (Kulkarni and Chauhan, 2015; Mizuno et al., 2019; Tsai et al., 2013). This observation aligns with the results in Fig. 7, which have already indicated the favorable absorption of interstitials by GBs. Fig. 14 further illustrates that the biased segregation of Ni interstitials is notably enhanced. This improvement effectively increases the absorption rate of total interstitials, contributing to the overall high defect absorption rate at GBs.

Finally, it is important to discuss the influence of temperature on the GB resistance to radiation damage in MPEAs. As previously mentioned, the simulations conducted in this study are performed at a temperature lower than typical radiation conditions to eliminate the complicating interference of temperature effects. The results obtained under these low-temperature simulations would serve as the baseline for further investigation into high-temperature collision cascades (Ma et al., 2023). With an increase in temperature, both the properties of GBs and defects undergo changes. On one hand, the GB structure becomes more disordered thereby enhances GB diffusion (Frolov et al., 2013a, 2013b; Rajeshwari et al., 2020), and the relaxation of GB structure becomes easier, allowing the GB to accommodate more defects (Li et al., 2022b, 2023e, 2022c; Ma et al., 2023). On the other hand, bulk diffusion of defects, especially the interstitial atoms, is enhanced. This enhanced bulk diffusion not only promotes defect recombination in the grain interior but also leads to more defects migrating to GBs (Li et al., 2023e, 2022c; Zhang et al., 2012). While these changes are beneficial for improving GB sink strength, their combining influence on irradiation damage is still hard to predict.

As revealed in the present work and supported by previous studies (Li et al., 2023a), the difference between interstitial and vacancy segregation energy is also an important factor in radiation damage. The gap between interstitial and vacancy segregation energies may widen, resulting in more sessile vacancies in the grain interior and potentially increasing radiation damage. These influences are uncertain and sensitive to GB type and composition (Utt et al., 2020; Yang et al., 2018; Zhang et al., 2023b). For MPEAs, the influence of temperature on GB sink strength may be weakened since the GBs are inherently disorder (Tan et al., 2021; Yang et al., 2020) Simultaneously, the sluggish diffusion effect may reduce the kinetic differences between interstitials and vacancies (Jiang et al., 2021; Tsai et al., 2013; Vaidya et al., 2018), thereby facilitating their recombination. In summary, the influence of temperature is highly sensitive to GB type and composition, requiring additional research and systematic analysis.

5. Conclusion

In this study, we investigated the impact of GBs on irradiation damage in pure Ni and NiCoCr MPEA. Through the analysis of defects induced by collision cascades in bicrystal systems with different GB structures, we explored the relationship between GB properties (GB excess energy, GB excess volume, and defect segregation energy at GBs) and the characteristics of irradiation damage (number and

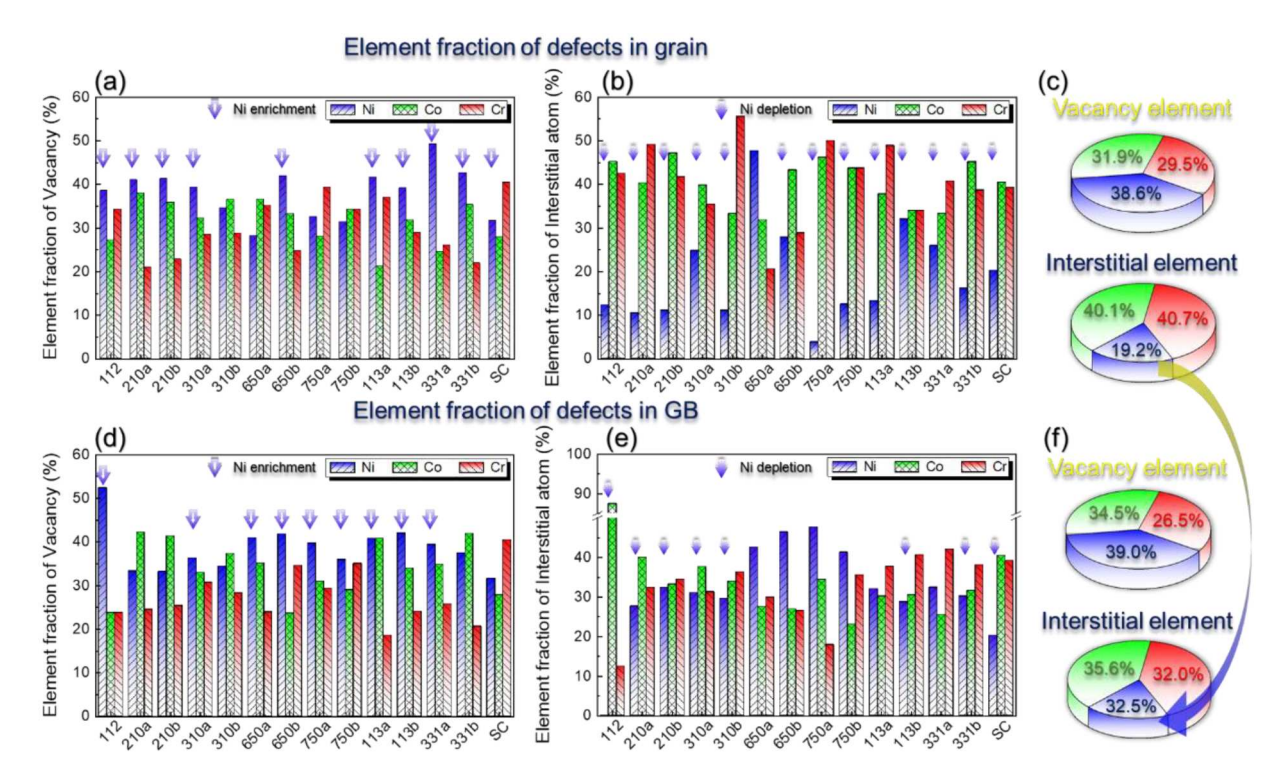


Fig. 14. Element fraction of the irradiation defects in (a–c) the grain and (d–f) the GB. (a) The element fraction of the surviving vacancies in the grain. (b) The element fraction of the surviving interstitials in the grain. (c) The average element fraction of the surviving defects in the grain of all models. (d) The element fraction of the segregated vacancies in the GB. (e) The element fraction of the segregated interstitials in the GB. (f) The average element fraction of the segregated defects in the GB of all models.

distribution of irradiation-induced vacancies and interstitials). The findings demonstrate that GBs in NiCoCr can reduce more surviving defects compared to pure Ni, highlighting the effectiveness of GBs as anti-irradiation microstructures in NiCoCr MPEAs.

The analysis of GB properties and irradiation defects reveals that GB resistance to irradiation damage is influenced by both the overall GB energetic state (GB excess energy and defect segregation energy) and the energy difference between interstitial and vacancy segregation. A unique exponent function between the defect absorption rate at GB and the GB energetic state is uncovered for both Ni and NiCoCr. It is found that the defect absorption rate can be improved by increasing the overall GB energetic state, as well as the biased reduction of interstitial segregation energy, providing a feasible strategy to enhance the GB resistance to irradiation damage in MPEAs.

In contrast to pure Ni, the significant lattice distortion in MPEA leads to GB disordering, resulting in higher GB entropy. This essentially reduces the GB energetic state, particularly the interstitial segregation energy, and significantly narrows down the energy difference between vacancy and interstitial segregation. This phenomenon is beneficial for improving the recombination of point defects, a key factor in enhancing the radiation resistance of GBs in MPEA. Additionally, the analysis of element fraction in residual defects after irradiation further reveals the promoted biased segregation of Ni interstitials in NiCoCr. This behavior not only contributes to the elevated defect absorption level but also induces Ni enrichment in GBs. These results unveil the origins of GB resistance to irradiation damage and underscore the crucial role of lattice distortion and composition in this resistance.

By purposefully tuning the composition state and structural disorder of GBs to tailor the GB energetic state, it becomes possible to rationally design alloys with improved radiation tolerance.

CRediT authorship contribution statement

Fusheng Tan: Writing – review & editing, Writing – original draft. **Jia Li:** Writing – original draft. **Bin Liu:** Funding acquisition, Formal analysis. **Peter K Liaw:** Methodology, Software, Data curation, Writing – original draft, Visualization, Investigation, Writing – review & editing. **Qihong Fang:** Writing – review & editing, Writing – original draft, Visualization.

Declaration of competing interest

The authors declare that they have no known competing financial interests or personal relationships that could have appeared to influence the work reported in this paper.

Data availability

Data will be made available on request.

Acknowledgment

The authors would like to deeply appreciate the supports from National Natural Science Foundation of China (U2267252, 12372069, 12302083, and 12172123), Natural Science Foundation of Hunan Province (2022JJ20001), The Science and Technology Innovation Program of Hunan Province (2022RC1200), and The Postdoctoral Science Foundation of China (GZC20231312). PKL very much appreciates the support from the National Science Foundation (DMR-1611180, 1809640, and 2226508).

References

- Allen, T.R., Busby, J.T., Was, G.S., Kenik, E.A., 1998. On the mechanism of radiation-induced segregation in austenitic Fe-Cr-Ni alloys. J. Nucl. Mater. 255, 44–58. Aust. K.T., 1969. Grain boundary studies and their technological significance. Can. Metall. Ouart. 8, 173–178.
- Bai, X.M., Voter, A.F., Hoagland, R.G., Nastasi, M., Uberuaga, B.P., 2010. Efficient annealing of radiation damage near grain boundaries via interstitial emission. Science 327, 1631–1634.
- Bao, Q.F., Huang, M.S., Zhu, Y.X., Zhao, L., Li, Z.H., 2022. Abnormal interactions between high-speed edge dislocation and microvoid in BCC metals. Int. J. Plast. 148, 103125
- Barr, C.M., Nathaniel, J.E., Unocic, K.A., Liu, J.P., Zhang, Y., Wang, Y.Q., Taheri, M.L., 2018. Exploring radiation induced segregation mechanisms at grain boundaries in equiatomic CoCrFeNiMn high entropy alloy under heavy ion irradiation. Scr. Mater. 156, 80–84.
- Barron, P.J., Carruthers, A.W., Fellowes, J.W., Jones, N.G., Dawson, H., Pickering, E.J., 2020. Towards V-based high-entropy alloys for nuclear fusion applications. Scr. Mater. 176, 12–16.
- Baruffi, C., Brandl, C., 2023. Vacancy segregation and intrinsic coordination defects at (1 1 1) twist grain boundaries in diamond. Acta Mater. 260, 119253.
- Becquart, C.S., De Backer, A., Domain, C., 2019. Atomistic modeling of radiation damage in metallic alloys. In: Handbook of Mechanics of Materials. Springer Singapore.
- Bourasseau, E., Onofri, C., Ksibi, A., Iltis, X., Belin, R.C., Lapertot, G., 2022. Atomic structure of grain boundaries in UO₂ bicrystals: a coupled high resolution transmission electron microscopy/atomistic simulation approach. Scr. Mater. 206, 114191.
- Cantwell, P.R., Tang, M., Dillon, S.J., Luo, J., Rohrer, G.S., Harmer, M.P., 2014. Grain boundary complexions. Acta Mater. 62, 1-48.
- Cao, T.Q., Zhang, Q., Wang, L., Wang, L., Xiao, Y., Yao, J.H., Liu, H.Y., Ren, Y., Liang, J., Xue, Y.F., Li, X.Y., 2023. Dynamic deformation behaviors and mechanisms of CoCrFeNi high-entropy alloys. Acta Mater. 260, 119343.
- Chen, B., Li, S.Z., Zong, H.X., Ding, X.D., Sun, J., Ma, E.A., 2020a. Unusual activated processes controlling dislocation motion in body-centered-cubic high-entropy alloys. Proc. Natl. Acad. Sci. USA 117, 16199–16206.
- Chen, H.H., Zhao, Y.F., Zhang, J.Y., Wang, Y.Q., Li, G.Y., Wu, K., Liu, G., Sun, J., 2020b. He-ion irradiation effects on the microstructure stability and size-dependent mechanical behavior of high entropy alloy/Cu nanotwinned nanolaminates. Int. J. Plast. 133, 102839.
- Chen, Z., Wang, R., Shu, Y., Lin, Y., Liu, Z., Deng, H., Hu, W., Yang, T., 2023. The interactions between dislocations and displacement cascades in FeCoCrNi concentrated solid-solution alloy and pure Ni. J. Nucl. Mater. 576, 154286.
- Christodoulou, P.G., Zecevic, M., Lebensohn, R.A., Beyerlein, I.J., 2023. Role of grain boundary crystallography on void growth in FCC metals. Int. J. Plast. 171, 103803.
- Cooper, M.W.D., Gamble, K.A., Capolungo, L., Matthews, C., Andersson, D.A., Beeler, B., Stanek, C.R., Metzger, K., 2021. Irradiation-enhanced diffusion and diffusion-limited creep in U₃Si₂. J. Nucl. Mater. 555, 153129.
- Cui, Y.N., Po, G., Ghoniem, N., 2018a. Size-tuned plastic flow localization in irradiated materials at the submicron scale. Phys. Rev. Lett. 120, 215501.
- Cui, Y.N., Po, G., Ghoniem, N., 2018b. Suppression of localized plastic flow in irradiated materials. Scr. Mater. 154, 34–39.
- Cui, Y.N., Po, G., Ghoniem, N.M., 2018c. A coupled dislocation dynamics-continuum barrier field model with application to irradiated materials. Int. J. Plast. 104, 54–67.
- Deluigi, O.R., Pasianot, R.C., Valencia, F.J., Caro, A., Farkas, D., Bringa, E.M., 2021. Simulations of primary damage in a high entropy alloy: probing enhanced radiation resistance. Acta Mater. 213, 116951.
- Ding, Q.Q., Fu, X.Q., Chen, D.K., Bei, H.B., Gludovatz, B., Li, J.X., Zhang, Z., George, E.P., Yu, Q., Zhu, T., Ritchie, R.O., 2019. Real-time nanoscale observation of deformation mechanisms in CrCoNi-based medium- to high-entropy alloys at cryogenic temperatures. Mater. Today 25, 21–27.
- Dunn, A., Dingreville, R., Martinez, E., Capolungo, L., 2016. Identification of dominant damage accumulation processes at grain boundaries during irradiation in nanocrystalline α-Fe: a statistical study. Acta Mater. 110, 306–323.
- El-Atwani, O., Li, N., Li, M., Devaraj, A., Baldwin, J.K.S., Schneider, M.M., Sobieraj, D., Wrobel, J.S., Nguyen-Manh, D., Maloy, S.A., Martinez, E., 2019. Outstanding radiation resistance of tungsten-based high-entropy alloys. Sci. Adv. 5, eaav2002.
- Eleti, R.R., Chokshi, A.H., Shibata, A., Tsuji, N., 2020. Unique high-temperature deformation dominated by grain boundary sliding in heterogeneous necklace structure formed by dynamic recrystallization in HfNbTaTiZr BCC refractory high entropy alloy. Acta Mater. 183, 64–77.
- Elsener, A., Politano, O., Derlet, P.M., Van Swygenhoven, H., 2009. Variable-charge method applied to study coupled grain boundary migration in the presence of oxygen. Acta Mater. 57, 1988–2001.
- Fernández-Pello, D., Cerdeira, M.A., Suárez-Recio, J., González-Arrabal, R., Iglesias, R., González, C., 2022. Coexistence of a self-interstitial atom with light impurities in a tungsten grain boundary. J. Nucl. Mater. 560, 153481
- Field, K.G., Briggs, S.A., Hu, X.X., Yamamoto, Y., Howard, R.H., Sridharan, K., 2017. Heterogeneous dislocation loop formation near grain boundaries in a neutron-irradiated commercial FeCrAl alloy. J. Nucl. Mater. 483, 54–61.
- Field, K.G., Yang, Y., Allen, T.R., Busby, J.T., 2015. Defect sink characteristics of specific grain boundary types in 304 stainless steels under high dose neutron environments. Acta Mater. 89, 438–449.
- Fischer, F., Schmitz, G., Eich, S.M., 2019. A systematic study of grain boundary segregation and grain boundary formation energy using a new copper–nickel embedded-atom potential. Acta Mater. 176, 220–231.
- Forty, C.B.A., Karditsas, P.J., 2000. Uses of zirconium alloys in fusion applications. J. Nucl. Mater. 283, 607-610.
- Frolov, T., Divinski, S.V., Asta, M., Mishin, Y., 2013a. Effect of interface phase transformations on diffusion and segregation in high-angle grain boundaries. Phys. Rev. Lett. 110, 255502.
- Frolov, T., Olmsted, D.L., Asta, M., Mishin, Y., 2013b. Structural phase transformations in metallic grain boundaries. Nat. Commun. 4, 1899.
- Fu, H.L., Zhou, X., Xue, H.T., Li, X.Y., Lu, K., 2022. Breaking the purity-stability dilemma in pure Cu with grain boundary relaxation. Mater. Today 55, 66–73.
- Fujii, T., Hisada, Y., Tohgo, K., Shimamura, Y., 2020. Investigation on nucleation of intergranular stress corrosion cracking in austenitic stainless steel by in situ strain measurement. Mater. Sci. Eng. A 773, 138858.
- Gao, Z., Huang, J., Liu, H., Ge, W., Luo, F., Zhang, B., Liu, G., Sun, B., Shen, T., Xue, J., Wang, Y., Wang, C., 2023. Ultra-wide void denuded zone near composite grain boundary in micro-nano crystalline 304L steels. Scr. Mater. 232, 115497.

- George, E.P., Raabe, D., Ritchie, R.O., 2019. High-entropy alloys. Nat. Rev. Mater. 4, 515-534.
- Gludovatz, B., Hohenwarter, A., Catoor, D., Chang, E.H., George, E.P., Ritchie, R.O., 2014. A fracture-resistant high-entropy alloy for cryogenic applications. Science 345, 1153–1158.
- Gludovatz, B., Hohenwarter, A., Thurston, K.V.S., Bei, H.B., Wu, Z.G., George, E.P., Ritchie, R.O., 2016. Exceptional damage-tolerance of a medium-entropy alloy CrCoNi at cryogenic temperatures. Nat. Commun. 7, 10602.
- Gupta, V.K., Yoon, D.H., Meyer, H.M., Luo, J., 2007. Thin intergranular films and solid-state activated sintering in nickel-doped tungsten. Acta Mater. 55, 3131–3142. Han, J., Vitek, V., Srolovitz, D.J., 2016. Grain-boundary metastability and its statistical properties. Acta Mater. 104, 259–273.
- Hendy, M., Ponga, M., 2023. A multiscale and multiphysics framework to simulate radiation damage in nano-crystalline materials. J. Nucl. Mater. 578, 154347.
- Hoffman, A.K., Zhang, Y., Arivu, M., He, L., Sridharan, K., Wu, Y., Islamgaliev, R.K., Valiev, R.Z., Wen, H., 2023. Novel effects of grain size and ion implantation on grain boundary segregation in ion irradiated austenitic steel. Acta Mater. 246, 118714.
- Hung, C.Y., Vetterick, G., Hopkins, E., Balwin, J.K., Baldo, P., Kirk, M.A., Misra, A., Taheri, M.L., 2022. Insight into defect cluster annihilation at grain boundaries in an irradiated nanocrystalline iron. J. Nucl. Mater. 566, 153761.
- Ji, C.O., Cui, Y.A., Li, Y., Ghoniem, N., 2022. A concurrent irradiation-mechanics multiscale coupling model. J. Mech. Phys. Solids 167, 105005.
- Jiang, C., Swaminathan, N., Deng, J., Morgan, D., Szlufarska, I., 2014. Effect of grain boundary stresses on sink strength. Mater. Res. Lett. 2, 100-106.
- Jiang, J., Lu, Z., Shen, J., Wada, T., Kato, H., Chen, M.W., 2021. Decoupling between calorimetric and dynamical glass transitions in high-entropy metallic glasses. Nat. Commun. 12, 3843.
- Jiang, Z.J., He, J.Y., Wang, H.Y., Zhang, H.S., Lu, Z.P., Dai, L.H., 2016. Shock compression response of high entropy alloys. Mater. Res. Lett. 4, 226-232.
- Kelchner, C.L., Plimpton, S.J., Hamilton, J.C., 1998. Dislocation nucleation and defect structure during surface indentation. Phys. Rev. B 58, 11085-11088.
- Knaster, J., Moeslang, A., Muroga, T., 2016. Materials research for fusion. Nat. Phys. 12, 424–434.
- Kulkarni, K., Chauhan, G.P.S., 2015. Investigations of quaternary interdiffusion in a constituent system of high entropy alloys. AIP Adv. 5, 097162.
- Kumar, N.A.P.K., Li, C., Leonard, K.J., Bei, H., Zinkle, S.J., 2016. Microstructural stability and mechanical behavior of FeNiMnCr high entropy alloy under ion irradiation. Acta Mater. 113, 230–244.
- Kusama, T., Omori, T., Saito, T., Kise, S., Tanaka, T., Araki, Y., Kainuma, R., 2017. Ultra-large single crystals by abnormal grain growth. Nat. Commun. 8, 354. Lee, J., Terner, M., Jun, S., Hong, H.U., Copin, E., Lours, P., 2020. Heat treatments design for superior high-temperature tensile properties of Alloy 625 produced by selective laser melting. Mater. Sci. Eng. A 790, 139720.
- Lee, J.U., Kim, S.H., Kim, Y.J., Park, S.H., 2018. Effects of homogenization time on aging behavior and mechanical properties of AZ91 alloy. Mater. Sci. Eng. A 714, 49–58.
- Li, J., Chen, H.T., Fang, Q.H., Jiang, C., Liu, Y., Liaw, P.K., 2020. Unraveling the dislocation-precipitate interactions in high-entropy alloys. Int. J. Plast. 133, 102819. Li, J., Yang, X., Wang, P., An, Q., 2022a. Dynamic interactions between low-angle grain boundary and stacking fault tetrahedron in Ni-Fe solid solution alloys. J. Alloys Compd. 907, 164572.
- Li, J., Yang, X., Wang, P., An, Q., 2022b. Healing stacking fault tetrahedron in NiFe solid solution alloys through grain boundary migration. J. Nucl. Mater. 565, 153738.
- Li, J., Yang, X.H., Wang, P., Qian, Q., 2023a. Interactions between displacement cascades and grain boundaries in NiFe single-phase concentrated solid solution alloys. Nucl. Instrum. Meth. B 541, 322–332.
- Li, J.Y., Wu, Y.H., Bai, Z.W., Yu, W.S., Shen, S.P., 2023b. Nanostructure-property relation of σ5 grain boundary in HfNbZrTi high-entropy alloy under shear. J. Mater. Sci. 58, 6757–6774.
- Li, Q.J., Sheng, H., Ma, E., 2019. Strengthening in multi-principal element alloys with local-chemical-order roughened dislocation pathways. Nat. Commun. 10, 3563.
- Li, R., Li, Y., Liu, Y., Peng, Q., 2023c. The effect of grain boundary on irradiation resistance of CoCrCuFeNi high entropy alloy. Comp. Mater. Sci. 225, 112185.
- Li, W., Lyu, S., Chen, Y., Ngan, A.H.W., 2023d. Fluctuations in local shear-fault energy produce unique and dominating strengthening in metastable complex concentrated alloys. Proc. Natl. Acad. Sci. USA 120 e2209188120.
- Li, X., Ding, C., Zhang, Y., Xu, Y., Li, X., Wang, X., Fang, Q.F., Wu, X., Liu, C.S., 2023e. Vacancy accumulation mechanism at iron grain boundaries: the influence of grain boundary character and its coupling with grain size. J. Nucl. Mater. 579, 154386.
- Li, X., Li, X., Zhang, Y., Xu, Y., Wu, X., Wang, X., Liu, C.S., Fang, Q.F., 2022c. Radiation damage accumulation mechanisms at iron grain boundaries revealed by coupled atomic and coarse-grained simulations via the parameter-passing and structural feedback. J. Nucl. Mater. 572, 154092.
- Li, X.Y., Liu, W., Xu, Y.C., Liu, C.S., Fang, Q.F., Pan, B.C., Chen, J.L., Luo, G.N., Wang, Z.G., 2014. Principal physical parameters characterizing the interactions between irradiation-induced point defects and several tilt symmetric grain boundaries in Fe, Mo and W. J. Nucl. Mater. 444, 229–236.
- Li, X.Y., Liu, W., Xu, Y.C., Liu, C.S., Pan, B.C., Liang, Y.F., Fang, Q.F., Chen, J.L., Luo, G.N., Lu, G.H., Wang, Z.G., 2016. Radiation resistance of nano-crystalline iron: coupling of the fundamental segregation process and the annihilation of interstitials and vacancies near the grain boundaries. Acta Mater. 109, 115–127.
- Li, Z.J., Liu, Z.L., Zhuang, Z., Cui, Y.N., 2021. Temperature dependent deformation localization in irradiated tungsten. Int. J. Plast. 146, 103077.
- Lin, Y.P., Yang, T.F., Lang, L., Shan, C., Deng, H.Q., Hu, W.Y., Gao, F., 2020. Enhanced radiation tolerance of the Ni-Co-Cr-Fe high-entropy alloy as revealed from primary damage. Acta Mater. 196, 133–143.
- Liu, L., Chen, Y., Gao, N., Liu, Z., Gao, F., Hu, W., Deng, H., 2022. Molecular dynamic simulations of displacement cascades in tungsten and tungsten–rhenium alloys: effects of grain boundary and/or σ phase. J. Nucl. Mater. 561, 153543.
- Liu, X.F., Tian, Z.L., Zhang, X.F., Chen, H.H., Liu, T.W., Chen, Y., Wang, Y.J., Dai, L.H., 2020. "Self-sharpening" tungsten high-entropy alloy. Acta Mater. 186, 257–266.
- Lu, C.Y., Niu, L.L., Chen, N.J., Jin, K., Yang, T.N., Xiu, P.Y., Zhang, Y.W., Gao, F., Bei, H.B., Shi, S., He, M.R., Robertson, L.M., Weber, W.J., Wang, L.M., 2016. Enhancing radiation tolerance by controlling defect mobility and migration pathways in multicomponent single-phase alloys. Nat. Commun. 7, 13564.
- Lu, E., Zhao, J., Makkonen, I., Mizohata, K., Li, Z., Hua, M., Djurabekova, F., Tuomisto, F., 2021. Enhancement of vacancy diffusion by C and N interstitials in the equiatomic FeMnNiCoCr high entropy alloy. Acta Mater. 215, 117093.
- Lu, K., Lu, L., Suresh, S., 2009. Strengthening materials by engineering coherent internal boundaries at the nanoscale. Science 324, 349-352.
- Lu, S.J., Kan, Q.H., Zaiser, M., Li, Z.H., Kang, G.Z., Zhang, X., 2022. Size-dependent yield stress in ultrafine-grained polycrystals: a multiscale discrete dislocation dynamics study. Int. J. Plast. 149, 103183.
- Luo, J., Zhou, N.X., 2023. High-entropy grain boundaries. Commun. Mater. 4, 7.
- Ma, P.W., Mason, D.R., Van Boxel, S., Dudarev, S.L., 2023. Athermal evolution of nanocrystalline tungsten driven by irradiation. J. Nucl. Mater. 586, 154662.
- Ma, S., Asl, K.M., Tansarawiput, C., Cantwell, P.R., Qi, M., Harmer, M.P., Luo, J., 2012. A grain boundary phase transition in Si-Au. Scr. Mater. 66, 203-206.
- Manna, M., Pal, S., 2023. Molecular dynamics simulation for radiation response of Nb bicrystal having Σ13, Σ29, and Σ85 grain boundary. J. Appl. Phys. 133, 154662. Marwick, A.D., Clark, G.J., 1989. Ion implantation in high-Tc superconductors. Nucl. Inst. Methods Phys. Res. B 37–38, 910–916.
- Marwick, A.D., Piller, R.C., 1977. The effect of point defect fluxes on radiation enhanced diffusion in nickel. Radiat. Eff. 33, 245-250.
- Medlin, D.L., Hattar, K., Zimmerman, J.A., Abdeljawad, F., Foiles, S.M., 2017. Defect character at grain boundary facet junctions: analysis of an asymmetric $\Sigma = 5$ grain boundary in Fe. Acta Mater. 124, 383–396.
- Meiners, T., Frolov, T., Rudd, R.E., Dehm, G., Liebscher, C.H., 2020. Observations of grain-boundary phase transformations in an elemental metal. Nature 579, 375–378.
- Miracle, D.B., Senkov, O.N., 2017. A critical review of high entropy alloys and related concepts. Acta Mater. 122, 448-511.
- Mizuno, M., Sugita, K., Araki, H., 2019. Defect energetics for diffusion in CrMnFeCoNi high-entropy alloy from first-principles calculations. Comput. Mater. Sci. 170, 109163.
- Moghaddam, A.O., Cabot, A., Trofimov, E.A., 2021. Does the pathway for development of next generation nuclear materials straightly go through high-entropy materials? Int. J. Refract. Met. Hard Mater. 97, 105504.
- Mohr, M., Daccache, L., Horvat, S., Brühne, K., Jacob, T., Fecht, H.J., 2017. Influence of grain boundaries on elasticity and thermal conductivity of nanocrystalline diamond films. Acta Mater. 122, 92–98.

Moladje, G.F.B., Thuinet, L., Becquart, C.S., Legris, A., 2022. Radiation induced segregation near dislocations and symmetric tilt grain boundaries in Fe-Cr alloys: a phase-field study. Acta Mater. 225, 117523.

Naeem, M., He, H.Y., Zhang, F., Huang, H.L., Harjo, S., Kawasaki, T., Wang, B., Lan, S., Wu, Z.D., Wang, F., Wu, Y., Lu, Z.P., Zhang, Z.W., Liu, C.T., Wang, X.L., 2020. Cooperative deformation in high-entropy alloys at ultralow temperatures. Sci. Adv. 6, eaax4002.

Nordlund, K., Ghaly, M., Averback, R.S., Caturla, M., de la Rubia, T.D., Tarus, J., 1998. Defect production in collision cascades in elemental semiconductors and fcc metals. Phys. Rev. B 57, 7556–7570.

Olmsted, D.L., Holm, E.A., Foiles, S.M., 2009. Survey of computed grain boundary properties in face-centered cubic metals-II: grain boundary mobility. Acta Mater.

Orhan, O.K., Hendy, M., Ponga, M., 2023. Electronic effects on the radiation damage in high-entropy alloys. Acta Mater. 244, 118511.

Pan, Z., Rupert, T.J., 2016. Effect of grain boundary character on segregation-induced structural transitions. Phys. Rev. B 93, 134113.

Patel, D., Richardson, M.D., Jim, B., Akhmadaliev, S., Goodall, R., Gandy, A.S., 2020. Radiation damage tolerance of a novel metastable refractory high entropy alloy V2.5Cr1.2WMoCo0.04. J. Nucl. Mater. 531, 152005.

Peng, J., Li, L., Li, F., Liu, B., Zherebtsov, S., Fang, Q.H., Li, J., Stepanov, N., Liu, Y., Liu, F., Liaw, P.K., 2021. The predicted rate-dependent deformation behaviour and multistage strain hardening in a model heterostructured body-centered cubic high entropy alloy. Int. J. Plast. 145, 103073.

Plimpton, S., 1995. Fast parallel algorithms for short-range molecular dynamics. J. Comput. Phys. 117, 1–19.

Prithiv, T.S., Bhuyan, P., Pradhan, S.K., Sarma, V.S., Mandal, S., 2018. A critical evaluation on efficacy of recrystallization vs. strain induced boundary migration in achieving grain boundary engineered microstructure in a Ni-base superalloy. Acta Mater. 146, 187–201.

Pu, G., Lin, L., Ren, D., Gan, K., Liu, B., Ye, Z., Wang, Y., Zhang, K., Li, Z., Liu, B., 2022. Influence of tunable interfaces on radiation tolerance and nanomechanical behavior of homogeneous multi-nanolayered Al1.5CoCrFeNi high entropy alloy films. J. Nucl. Mater. 566, 153734.

Raabe, D., Herbig, M., Sandlöbes, S., Li, Y., Tytko, D., Kuzmina, M., Ponge, D., Choi, P.P., 2014. Grain boundary segregation engineering in metallic alloys: a pathway to the design of interfaces. Curr. Opin. Solid State Mater. Sci. 18, 253–261.

Ragone, D.V., 1995. Thermodynamics of Materials. JohnWiley & Sons. Scientific Reports.

Rajeshwari, K.S., Sankaran, S., Kumar, K.C.H., Rösner, H., Peterlechner, M., Esin, V.A., Divinski, S., Wilde, G., 2020. Grain boundary diffusion and grain boundary structures of a Ni-Cr-Fe-alloy: evidences for grain boundary phase transitions. Acta Mater. 195, 501–518.

Romero, R.A., Xu, S.Z., Jian, W.R., Beyerlein, I.J., Ramana, C.V., 2022. Atomistic simulations of the local slip resistances in four refractory multi-principal element alloys. Int. J. Plast. 149, 103157.

Roy, A., Singh, P., Balasubramanian, G., Johnson, D.D., 2022. Vacancy formation energies and migration barriers in multi-principal element alloys. Acta Mater. 226, 117611.

Sadeghilaridjani, M., Ayyagari, A., Muskeri, S., Hasannaeimi, V., Salloom, R., Chen, W.Y., Mukherjee, S., 2020. Ion irradiation response and mechanical behavior of reduced activity high entropy alloy. J. Nucl. Mater. 529, 151955.

Samaras, M., Derlet, P.M., Van Swygenhoven, H., Victoria, M., 2003. Movement of interstitial clusters in stress gradients of grain boundaries. Phys. Rev. B 68, 224111. Schneider, M., Laplanche, G., 2021. Effects of temperature on mechanical properties and deformation mechanisms of the equiatomic CrFeNi medium-entropy alloy. Acta Mater. 204. 116470.

Schweizer, P., Sharma, A., Pethö, L., Huszar, E., Vogl, L.M., Michler, J., Maeder, X., 2023. Atomic scale volume and grain boundary diffusion elucidated by in situ STEM. Nat. Commun. 14, 7601.

Senkov, O.N., Gorsse, S., Miracle, D.B., 2019. High temperature strength of refractory complex concentrated alloys. Acta Mater. 175, 394-405.

Senkov, O.N., Wilks, G.B., Miracle, D.B., Chuang, C.P., Liaw, P.K., 2010. Refractory high-entropy alloys. Intermetallics 18, 1758–1765.

Shi, T., Su, Z., Li, J., Liu, C., Yang, J., He, X., Yun, D., Peng, Q., Lu, C., 2022. Distinct point defect behaviours in body-centered cubic medium-entropy alloy NbZrTi induced by severe lattice distortion. Acta Mater. 229, 117806.

Shim, J.H., Lee, H.J., Wirth, B.D., 2006. Molecular dynamics simulation of primary irradiation defect formation in Fe-10 %Cr alloy. J. Nucl. Mater. 351, 56–64. Smirnov, G., 2020. Non-Arrhenius diffusion in bcc titanium: vacancy-interstitialcy model. Phys. Rev. B 102, 184110.

Stukowski, A., 2010. Visualization and analysis of atomistic simulation data with OVITO-the open visualization tool. Model. Simul. Mater. Sci. Eng. 18, 015012. Su, Z.X., Ding, J., Song, M., Jiang, L., Shi, T., Li, Z.M., Wang, S., Gao, F., Yun, D., Ma, E., Lu, C.Y., 2023. Enhancing the radiation tolerance of high-entropy alloys via

solute-promoted chemical heterogeneities. Acta Mater. 245, 118662.
Suzuki, A., Mishin, Y., 2005. Atomic mechanisms of grain boundary diffusion: low versus high temperatures. J. Mater. Sci. 40, 3155–3161.

Svoboda, J., Fischer, F.D., Fratzl, P., 2006. Diffusion and creep in multi-component alloys with non-ideal sources and sinks for vacancies. Acta Mater. 54, 3043–3053. Swalin, R.A., Rice, S.A., 1963. Thermodynamics of solids. Phys. Today 16, 72.

Takahashi, H., Hashimoto, N., 1993. Radiation-induced segregation and grain boundary migration in Fe-Cr-Ni model alloy under irradiation. Mater. Trans. 34, 1027–1030

Tan, F.S., Li, J., Feng, H., Fang, Q.H., Jiang, C., Liu, Y., Liaw, P.K., 2021. Entropy-induced transition on grain-boundary migration in multi-principal element alloys. Scr. Mater. 194, 113668.

Tandoc, C., Hu, Y.J., Qi, L., Liaw, P.K., 2023. Mining of lattice distortion, strength, and intrinsic ductility of refractory high entropy alloys. NPJ Comput. Mater. 9, 53. Tiwari, S., Tucker, G.J., McDowell, D.L., 2019. The effect of hydrostatic pressure on the shear deformation of Cu symmetric tilt interfaces. Int. J. Plast. 118, 87–104. Tsai, K.Y., Tsai, M.H., Yeh, J.W., 2013. Sluggish diffusion in Co-Cr-Fe-Mn-Ni high-entropy alloys. Acta Mater. 61, 4887–4897.

Tucker, G.J., McDowell, D.L., 2011. Non-equilibrium grain boundary structure and inelastic deformation using atomistic simulations. Int. J. Plast. 27, 841–857. Tuomisto, F., Makkonen, I., Heikinheimo, J., Granberg, F., Djurabekova, F., Nordlund, K., Velisa, G., Bei, H., Xue, H., Weber, W.J., Zhang, Y., 2020. Segregation of Ni at early stages of radiation damage in NiCoFeCr solid solution alloys. Acta Mater. 196, 44–51.

Utt, D., Stukowski, A., Albe, K., 2020. Grain boundary structure and mobility in high-entropy alloys: a comparative molecular dynamics study on a Sigma 11 symmetrical tilt grain boundary in face-centered cubic CuNiCoFe. Acta Mater. 186, 11–19.

Vaidya, M., Pradeep, K.G., Murty, B.S., Wilde, G., Divinski, S.V., 2018. Bulk tracer diffusion in CoCrFeNi and CoCrFeMnNi high entropy alloys. Acta Mater. 146, 211–224.

van Beers, P.R.M., Kouznetsova, V.G., Geers, M.G.D., Tschopp, M.A., McDowell, D.L., 2015. A multiscale model of grain boundary structure and energy: from atomistics to a continuum description. Acta Mater. 82, 513–529.

Wang, F.L., Balbus, G.H., Xu, S.Z., Su, Y.Q., Shin, J., Rottmann, P.F., Knipling, K.E., Stinville, J.C., Mills, L.H., Senkov, O.N., Beyerlein, I.J., Pollock, T.M., Gianola, D. S., 2020. Multiplicity of dislocation pathways in a refractory multiprincipal element alloy. Science 370, 95–101.

Wang, X.Y., Gao, N., Setyawan, W., Xu, B., Liu, W., Wang, Z.G., 2017. Effect of irradiation on mechanical properties of symmetrical grain boundaries investigated by atomic simulations. J. Nucl. Mater. 491, 154–161.

Wang, Y.Z., Wang, Y.J., 2022. Disentangling diffusion heterogeneity in high-entropy alloys. Acta Mater. 224, 117527.

Wang, Z.C., Saito, M., McKenna, K.P., Gu, L., Tsukimoto, S., Shluger, A.L., Ikuhara, Y., 2011. Atom-resolved imaging of ordered defect superstructures at individual grain boundaries. Nature 479, 380–383.

Wei, D.X., Gong, W., Tsuru, T., Lobzenko, I., Li, X.Q., Harjo, S., Kawasaki, T., Do, H.S., Bae, J.W., Wagner, C., Laplanche, G., Koizumi, Y., Adachi, H., Aoyagi, K., Chiba, A., Lee, B.J., Kim, H.S., Kato, H., 2022. Si-addition contributes to overcoming the strength-ductility trade-off in high-entropy alloys. Int. J. Plast. 159, 103443.

Wei, J.K., Feng, B., Ishikawa, R., Yokoi, T., Matsunaga, K., Shibata, N., Ikuhara, Y., 2021. Direct imaging of atomistic grain boundary migration. Nat. Mater. 20, 951–955.

Wen, W., Kohnert, A., Kumar, M.A., Capolungo, L., Tomé, C.N., 2020. Mechanism-based modeling of thermal and irradiation creep behavior: an application to ferritic/martensitic HT9 steel. Int. J. Plast. 126, 102633.

Wharry, J.P., Was, G.S., 2014. The mechanism of radiation-induced segregation in ferritic-martensitic alloys. Acta Mater. 65, 42-55.

- Wu, Z.F., Xu, L.D., Chen, H.Q., Liang, Y.X., Du, J.L., Wang, Y.F., Zhang, S.L., Cai, X.C., Sun, B.R., Zhang, J., Shen, T.D., Wang, J., Fu, E.G., 2022. Significant suppression of void swelling and irradiation hardening in a nanograined/nanoprecipitated 14YWT-ODS steel irradiated by helium ions. J. Nucl. Mater. 559, 153418.
- Xiao, X.Z., Chen, L.R., Yu, L., Duan, H.L., 2019. Modelling nano-indentation of ion-irradiated FCC single crystals by strain-gradient crystal plasticity theory. Int. J. Plast. 116, 216–231.
- Xie, R., Xu, C., Tian, X., Wang, Q., Jiang, W., Fan, H., 2023. Interaction between basal edge/mixed(a)dislocations and point defects in zirconium. Int. J. Plast. 171, 103815
- Xiong, Y.X., Zhang, J., Ma, S.H., Huang, S.S., Xu, B., Zhao, S.J., 2023. Multiscale modeling of irradiation-induced defect evolution in BCC multi principal element alloys. J. Alloys Compd. 953, 170084.
- Xu, C., Tian, X., Jiang, W., Wang, Q., Fan, H., 2024. The sink efficiency of symmetric tilt grain boundary under displacement cascade in zirconium. J. Nucl. Mater. 591, 154911.
- Xu, C.L., Tian, X.B., Jiang, W.T., Wang, Q.Y., Fan, H.D., 2022. Atomistic migration mechanisms of [1210] symmetric tilt grain boundaries in magnesium. Int. J. Plast. 156, 103362.
- Yang, T., Zhao, Y.L., Li, W.P., Yu, C.Y., Luan, J.H., Lin, D.Y., Fan, L., Jiao, Z.B., Liu, W.H., Liu, X.J., Kai, J.J., Huang, J.C., Liu, C.T., 2020. Ultrahigh-strength and ductile superlattice alloys with nanoscale disordered interfaces. Science 369, 427–432.
- Yang, T.F., Xia, S.Q., Guo, W., Hu, R., Poplawsky, J.D., Sha, G., Fang, Y., Yan, Z.F., Wang, C.X., Li, C.Y., Zhang, Y., Zinkle, S.J., Wang, Y.G., 2018. Effects of temperature on the irradiation responses of Al0.1CoCrFeNi high entropy alloy. Scr. Mater. 144, 31–35.
- Zhang, B.B., Tang, Y.G., Mei, Q.S., Li, X.Y., Lu, K., 2022a. Inhibiting creep in nanograined alloys with stable grain boundary networks. Science 378, 659–663. Zhang, C.G., Zhou, W.H., Li, Y.G., Zeng, Z., Ju, X., 2015a. Primary radiation damage near grain boundary in bcc tungsten by molecular dynamics simulations. J. Nucl. Mater. 458, 138–145.
- Zhang, Q., Niu, R., Liu, Y., Jiang, J., Xu, F., Zhang, X., Cairney, J.M., An, X., Liao, X., Gao, H., Li, X., 2023a. Room-temperature super-elongation in high-entropy alloy nanopillars. Nat. Commun. 14, 7469.
- Zhang, Y., Zuo, T.T., Tang, Z., Gao, M.C., Dahmen, K.A., Liaw, P.K., Lu, Z.P., 2014. Microstructures and properties of high-entropy alloys. Prog. Mater. Sci. 61, 1–93. Zhang, Y.F., Huang, H.C., Millett, P.C., Tonks, M., Wolf, D., Phillpot, S.R., 2012. Atomistic study of grain boundary sink strength under prolonged electron irradiation. J. Nucl. Mater. 422, 69–76.
- Zhang, Y.W., Stocks, G.M., Jin, K., Lu, C.Y., Bei, H.B., Sales, B.C., Wang, L.M., Beland, L.K., Stoller, R.E., Samolyuk, G.D., Caro, M., Caro, A., Weber, W.J., 2015b. Influence of chemical disorder on energy dissipation and defect evolution in concentrated solid solution alloys. Nat. Commun. 6, 8736.
- Zhang, Z.P., Huang, Q.S., Zhou, H.F., 2023b. High-entropy alloy nanocrystals with low-angle grain boundary for superb plastic deformability and recoverability. Int. J. Plast. 167, 103679.
- Zhang, Z.R., Armstrong, D.E.J., Grant, P.S., 2022b. The effects of irradiation on CrMnFeCoNi high-entropy alloy and its derivatives. Prog. Mater. Sci. 123, 100807. Zhang, Z.R., Zhang, H., Tang, Y., Zhu, L., Ye, Y.C., Li, S., Bai, S.X., 2017. Microstructure, mechanical properties and energetic characteristics of a novel high-entropy alloy HfZrTiTa. Mater. Des. 133, 435–443.
- Zhao, H., Cao, J., Wang, J., Jia, L., Dou, Y., Pan, C., He, X., 2023. Thermodynamic behavior of Cr/W alloy elements on α-Fe grain boundaries. At. Energy Sci. Technol. 57, 189–198.
- Zhao, S., Xiong, Y., Ma, S., Zhang, J., Xu, B., Kai, J.J., 2021. Defect accumulation and evolution in refractory multi-principal element alloys. Acta Mater. 219, 117233. Zhao, S.J., 2020. Defect properties in a VTaCrW equiatomic high entropy alloy (HEA) with the body centered cubic (bcc) structure. J. Mater. Sci. Technol. 44, 133–139.
- Zhao, S.J., Egami, T., Stocks, G.M., Zhang, Y.W., 2018. Effect of d electrons on defect properties in equiatomic NiCoCr and NiCoFeCr concentrated solid solution alloys. Phys. Rev. Mater. 2, 013602.
- Zheng, H., Li, X.G., Tran, R., Chen, C., Horton, M., Winston, D., Persson, K.A., Ong, S.P., 2020. Grain boundary properties of elemental metals. Acta Mater. 186, 40–49. Zheng, X.R., Kong, X.S., Li, X., Zhang, Y., Liu, C.S., 2023. The structure and energy of symmetric tilt grain boundaries in tungsten. J. Nucl. Mater. 581, 154442. Zhou, N.X., Hu, T., Huang, J.J., Luo, J., 2016a. Stabilization of nanocrystalline alloys at high temperatures via utilizing high-entropy grain boundary complexions. Scr. Mater. 124, 160–163.
- Zhou, X., Li, X.Y., Lu, K., 2018. Enhanced thermal stability of nanograined metals below a critical grain size. Science 360, 526-530.
- Zhou, X., Marchand, D., McDowell, D.L., Zhu, T., Song, J., 2016b. Chemomechanical origin of hydrogen trapping at grain boundaries in fcc metals. Phys. Rev. Lett. 116, 075502.
- Zhou, Z., Xie, H., Lu, G.H., 2022. Interaction between disclinated non-equilibrium grain boundaries and radiation-induced interstitial/vacancy in tungsten. Nucl. Fusion 62, 126031.
- Zhu, H., Qin, M., Wei, T., Davis, J., Ionescu, M., 2023. Atomic-scale study of He ion irradiation-induced clustering in α-Zirconium. Acta Mater. 244, 118584. Zhu, Q., Samanta, A., Li, B., Rudd, R.E., Frolov, T., 2017. Predicting phase behavior of grain boundaries with evolutionary search and machine learning. Nat.
- Commun. 9, 467. Zhu, Y.C., Luo, J., Guo, X., Xiang, Y., Chapman, S.J., 2018. Role of grain boundaries under long-time radiation. Phys. Rev. Lett. 120, 222501.
- Ziegler, J.F., Biersack, J.P., 1985. The stopping and range of ions in matter. In: Bromley, D.A. (Ed.), Treatise on Heavy-Ion Science: Volume 6: Astrophysics, Chemistry, and Condensed Matter. Springer US, Boston, MA, pp. 93–129.
- Zinkle, S.J., Busby, J.T., 2009. Structural materials for fission & fusion energy. Mater. Today 12, 12–19.